Title
Interaction of the westerlies with the Tibetan Plateau in determining the Mei-Yu termination

Journal
Journal of Climate, 33(1)

ISSN
0894-8755

Authors
Kong, W
Chiang, JCH

Publication Date
2020

DOI
10.1175/JCLI-D-19-0319.1

Peer reviewed

Interaction of the westerlies with the Tibetan Plateau in determining the mei-yu termination

Wenwen Kong[1] and John C. H. Chiang

Department of Geography and Berkeley Atmospheric Sciences Center,

University of California, Berkeley CA

Revised for Journal of Climate, September 2019

[1] *Corresponding author address:*
Wenwen Kong,
531 McCone Hall, University of California, Berkeley, CA, 94720-4740
wenwen.kong@berkeley.edu

Early Online Release: This preliminary version has been accepted for publication in *Journal of Climate*, may be fully cited, and has been assigned DOI 10.1175/JCLI-D-19-0319.1. The final typeset copyedited article will replace the EOR at the above DOI when it is published.

Abstract

This study explores how the termination of the mei-yu is dynamically linked to the westerlies impinging on the Tibetan Plateau. It is found that the mei-yu stage terminates when the maximum upper tropospheric westerlies shift beyond the northern edge of the Plateau, around $40°N$. This termination is accompanied by the disappearance of tropospheric northerlies over northeastern China. The link between the transit of the jet axis across the northern edge of the Plateau, the disappearance of northerlies, and termination of mei-yu holds on a range of timescales from interannual through seasonal and pentad. Diagnostic analysis indicates that the weakening of meridional moisture contrast and meridional wind convergence, mainly resulting from the disappearance of northerlies, causes the demise of the mei-yu front.

The authors propose that the westerlies migrating north of the Plateau and consequent weakening of the extratropical northerlies triggers mei-yu termination. Model simulations are employed to test the causality between the jet and the orographic downstream northerlies by repositioning the northern edge of the Plateau. As the Plateau edge extends northward, orographic forcing on the westerlies strengthens, leading to persistent strong downstream northerlies and a prolonged mei-yu. Idealized simulations with a dry dynamical core further demonstrate the dynamical link between the weakening of orographically forced downstream northerlies with the positioning of the jet from south to north of the Plateau. Changes in the magnitude of orographically forced stationary waves are proposed to explain why the downstream northerlies disappear when the jet axis migrates beyond the northern edge of the Plateau.

Accepted for publication in *Journal of Climate*. DOI 10.1175/JCLI-D-19-0319.1.

1. Introduction

The mei-yu (also known as changma in Korea and baiu in Japan) is a quasi-stationary rain belt extending from central eastern China to Japan, establishing around mid-June and disappearing around mid-July. The dynamics of the mei-yu are intimately tied to the westerlies impinging on the Tibetan Plateau. In particular, the synchronous relationship between the latitudinal position of westerlies over the Tibetan Plateau and the spatial pattern of the East Asian summer rain belt has long been recognized (Liang and Wang, 1998; Molnar et al., 2010; Murakami, 1951; Schiemann et al., 2009; Staff Members of the Section of Synoptic and Dynamic Meteorology, 1958; Yeh et al., 1959). For example, Schiemann et al (2009) note that the westerly jet migrates onto the Tibetan Plateau in May, corresponding to the pre-mei-yu in southeastern China; the westerly jet reaches the northern edge of the Plateau in June, timed to the mei-yu over central eastern China; as the jet migrates well north of the Plateau in July-August, midsummer occurs and brings more rainfall over northeastern China. Decreased summer rains over the Yangtze River Valley – the region dominated by the mei-yu – have been argued to be associated with the poleward displacement of westerlies in East Asia, and vice versa (e.g. Li and Zhang, 2014). Recent studies further suggest that the meridional positioning of the Asian westerly jet relative to the Tibetan Plateau controls the timing and duration of the mei-yu in both past (Chiang et al., 2015; Kong et al., 2017) and present (Chiang et al., 2017) climates.

A variety of mechanisms have been proposed for how the westerlies modulate the mei-yu. Japanese meteorologists noted that the demise of the baiu is associated with the establishment of an anticyclone over Japan around August, the latter being part of an

Accepted for publication in *Journal of Climate*. DOI 10.1175/JCLI-D-19-0319.1.

eastward propagating wave train – the so-called "Silk Road Pattern" (Enomoto et al., 2003). Subsequent studies suggest that the interannual variation of the East Asian Summer Monsoon (EASM) is closely associated with the "Silk Road Pattern" (Hsu and Lin, 2007; Kosaka et al., 2011). Li and Lu (2017) suggest that increased precipitation in the Yangtze River Basin is linked to northeasterly anomalies to the north of the region. They argue that the northeasterly anomaly in the lower troposphere is associated with the cyclonic anomaly over East Asia in the upper troposphere, and that the latter is induced by the "Silk Road Pattern" along the westerly jet. In fact, behavior of the "Silk Road Pattern" is closely linked to the meridional position of Asian westerlies (Hong and Lu, 2016; Hong et al., 2017). For instance, Hong and Lu (2016) suggest that when the jet is displaced southwards, the "Silk Road Pattern" tends to present as cyclonic anomalies over East Asia, and vice versa. Hong et al. (2017) further demonstrate that the "Silk Road Pattern" is more pronounced when the jet is located to north of the Tibetan Plateau. Taken together, these studies suggest that westerlies might affect the mei-yu through modulating the variation of the "Silk Road Pattern".

On the other hand, precipitation over central eastern China during the mei-yu exhibits strong correlation with ascending motion and horizontal warm advection in the mid-troposphere (e.g. Sampe and Xie, 2010). This strong correlation led Sampe and Xie (2010) to conclude that the westerly jet anchors the mei-yu rain band via the advection of warm air from the southeastern flank of the Tibetan Plateau, which is then lifted upwards over East Asia, thereby inducing convection. This argument attributes the demise of the mei-yu to the northward migration of the jet away from the maximum mid-tropospheric

Accepted for publication in *Journal of Climate*. DOI 10.1175/JCLI-D-19-0319.1.

89 temperature center; this interpretation is further supported by studies on variations of East
90 Asian summer rainfall at interannual timescales (Kosaka et al., 2011).

91 A different view of the role of the westerlies on the mei-yu was postulated by
92 Molnar et al. (2010). They focus on the effect of the westerlies impinging on the Tibetan
93 Plateau in altering the downstream circulation, specifically producing a locus of moisture
94 convergence that defines the mei-yu rainband. In this view, the demise of the mei-yu
95 rainband is dynamically tied to the northward seasonal migration of the westerlies from
96 south to north of the Plateau: when the core of the westerlies migrates off the Plateau, the
97 mechanical forcing of the Plateau disappears, and so does the mei-yu rainband. From an
98 energetic and moisture budget perspective, Chen and Bordoni (2014) argued that the
99 extratropical northerlies downstream of the Tibetan Plateau are crucial in maintaining the
100 mei-yu front via advecting dry enthalpy and strengthening the moisture convergence over
101 central eastern China.

102 The above studies suggested different processes for how the westerlies affect the
103 mei-yu. Although the origins of these mechanisms are independent, they consistently
104 indicate the meridional position of the westerly jet relative to the Tibetan Plateau is key
105 to formation and maintenance of the mei-yu. However, how this dynamically relates to
106 the demise of the mei-yu has not been examined in detail; this is the focus of this paper[ψ].
107 Furthermore, since the termination of the mei-yu is abrupt, it raises the question of
108 whether a latitude threshold in terms of jet position exists over the Plateau that triggers
109 the mei-yu termination. A recent modeling study on seasonal transitions of the jet and of

[ψ] As mentioned at the beginning of this section, the mei-yu is a more distinct rainfall stage of the EASM compared to midsummer. So we phrase the focus of this paper in terms of termination of the mei-yu, instead of onset of midsummer (aka post-Meiyu).

Accepted for publication in *Journal of Climate*. DOI 10.1175/JCLI-D-19-0319.1.

110 the EASM during the Holocene suggests exactly this (Kong et al., 2017). In that study,
111 the maximum in the 200mb westerly jet over the Tibetan Plateau ($80°E - 100°E$) was
112 found to be located at $40°N$ during the mei-yu onset, and the jet axis migrates northward
113 by one or two degrees when the mei-yu ends. $40°N$ is the latitude where the mean
114 Plateau elevation across $80°E - 100°E$ drops below 1.5 km, marking the northern edge
115 of the Plateau. It suggests that $40°N$ acts as this threshold, and mei-yu ends when the jet
116 core migrates to north of $40°N$.
117 In this study, we confirm previous findings (Kong et al., 2017) that the
118 termination of the mei-yu indeed coincides with the maximum upper tropospheric
119 westerlies over the Tibetan Plateau shifting north of $40°N$. We also find that these
120 changes are accompanied with disappearance of tropospheric northerlies over
121 northeastern China ($35° - 40°N$). We show that these concurrent behaviors hold from
122 climatology to interannual and synoptic timescales, which motivate us to hypothesize that
123 migration of the jet impinging over the Plateau to north of $40°N$ causes the weakening of
124 orographic downstream northerlies; and this weakening in northerlies over central-north
125 eastern China acts to terminate the mei-yu.
126 Mountains have long been held to be important in shaping the circulation and
127 climate in the Northern Hemisphere midlatitudes (Bolin, 1950; Broccoli and Manabe,
128 1992; Manabe and Terpstra, 1974). Model simulations have suggested that the presence
129 of the orography over Asia is essential for the existence of the Asian monsoon (Hahn and
130 Manabe, 1975; Kitoh, 2004; Park et al., 2012; Wong et al., 2018; Wu et al., 2012). A
131 widely-held view is that elevated sensible heating over the Tibetan Plateau drives the
132 EASM (Flohn, 1957; Li and Yanai, 1996; Wu et al., 2012; Yeh et al., 1959). However,

Accepted for publication in *Journal of Climate*. DOI 10.1175/JCLI-D-19-0319.1.

this view is challenged by studies that emphasized the role of mechanical influence of the Tibetan Plateau on its surrounding circulations (e.g. Molnar et al., 2010; Park et al., 2012; Staff Members of the Section of Synoptic and Dynamic Meteorology, 1958).

In this study, we argue that topographically-forced stationary waves provide a potential dynamical link between the westerlies impinging on the Tibetan Plateau and the downstream northerly response. In the midlatitudes, the linear response of the atmosphere to orographic forcing shows equatorward propagation of the stationary Rossby wave and the generation of low-level cyclonic motion downstream of the mountain (Cook and Held, 1992; Held, 1983; Hoskins and Karoly, 1981). Following these studies, we attribute variations of northerlies over northeastern China to changes in the strength of the cyclonic circulation downstream of the Plateau. We argue that migration of the jet to the north of the Plateau weakens the orographic forcing and thus weakens the cyclonic circulation, leading to weakening and even disappearance of the northerlies.

We describe the data, methodology and experiments in the next section. In section 3, we show how the climatological mean atmospheric circulation changes during the mei-yu termination. We then examine the variation of the mei-yu termination at interannual timescales and mei-yu-like rainfall patterns at synoptic scales in section 4. We explore how weakening of northerlies over central-northern eastern China affects the mei-yu termination in section 5. In section 6, we propose a hypothesis on the mei-yu termination and employ idealized simulations to test the response of northerlies and mei-yu termination to changes in the orographic forcing by perturbing the northern edge of the Tibetan Plateau. We then use the dry dynamical core of a general circulation model (GCM) to explore the change to the orographic downstream northerlies as the location of

Accepted for publication in *Journal of Climate*. DOI 10.1175/JCLI-D-19-0319.1.

156 westerlies changes from south to north of the Plateau (section 7). We close the paper with
157 summaries in section 8.
158
159 **2. Data, methods and experiments**
160 ***a. Data***
161 We use winds, geopotential height, temperature and specific humidity from the European
162 Centre for Medium-Range Weather Forecasts (ECMWF) Interim Re-Analysis (ERA-
163 Interim) products (Dee et al., 2011), spanning the 29-yr period from 1979 to 2007. Daily
164 fields are obtained by averaging the 6-hourly products mapped onto a 1°×1° grid on the
165 standard pressure levels.
166 As with Kong et al. (2017), we use the APHRO_MA_025deg_V1003R1 product
167 from the APHRODITE rain gauge data (Yatagai et al., 2009) to present summer rainfall
168 in East Asia. We focus on the period of 1979-2007 for consistency with the ERA-Interim
169 dataset.
170
171 ***b. Self-Organizing Maps***
172 Following Chiang et al. (2017) and Kong et al. (2017), we use the Self-Organizing Maps
173 (SOMs) (Kohonen, 2001; Kohonen et al., 1996) to objectively extract the seasonal
174 EASM rainfall stages, and identify the termination of the mei-yu. The SOMs is a neural
175 network-based cluster analysis that classifies a high-dimensional dataset into
176 representative patterns (Kohonen, 2001; Kohonen et al., 1996). This method has been
177 applied successfully to extract patterns of the El Nino-Southern Oscillation (Johnson,
178 2013) and the Northern and Southern Hemisphere teleconnections (Chang and Johnson,

Accepted for publication in *Journal of Climate*. DOI 10.1175/JCLI-D-19-0319.1.

2015; Johnson et al., 2008). It has also been used on the intraseasonal oscillation of the Indian summer monsoon (Chattopadhyay et al., 2008) and the East Asian-western North Pacific summer monsoon (Chu et al., 2012).

The SOMs analysis of the APHRODITE daily climatology used in this study is similar to Kong et al. (2017), to which the readers are referred for details. This study differs from Kong et al. (2017) in that we focus on a shorter period covering 1979-2007 and that we use the 9 day (instead of 5 day as in Kong et al. (2017)) running mean of daily climatology for the SOMs analysis.

c. Definition of Jet Position

We quantify the position of the westerly jet over the Plateau based on its axis at 200mb. We first zonally average the zonal wind at 200mb between $80°E$ and $100°E$, overlapping with the main body of the Tibetan Plateau. We then identify the location of the maximum zonal wind between $20°N$ to $50°N$ as the jet axis impinging on the Plateau. We restrict the search latitudes to $20°N$ to $50°N$ in order to exclude the potential identification of the polar front jet at higher latitudes.

d. Model Experiments

We use the National Center for Atmospheric Research's (NCAR) Community Earth System Model (CESM) version 1.2.2 (Hurrell et al., 2013). Previous work (Chiang et al., 2015; Kong et al., 2017) shows that this model simulates the seasonality of the EASM with fidelity. We design two sets of experiments: 1) Testing the behavior of the mei-yu under "northward-extended Plateau" scenarios, and 2) Testing responses of orographic

Accepted for publication in *Journal of Climate*. DOI 10.1175/JCLI-D-19-0319.1.

downstream northerlies by perturbing relative positioning of westerlies to the Plateau in idealized simulations with a dry dynamical core.

For the "northward-extended Plateau" simulations (section 7), we use the F_1850_CAM5 component set (Vertenstein et al., 2011), which includes the coupler, active atmosphere, land, and ice components, and a data ocean model with fixed sea surface temperature (SST). The atmospheric component of the CESM1 is the Community Atmosphere Model version 5 (CAM5) (Neale et al., 2010) at 0.9°×1.25° horizontal resolution and with 30 vertical layers. We conduct four simulations, namely "Plateau_control", "Plateau_3deg", "Plateau_6deg", and "Plateau_10deg". The only difference among these simulations is the meridional dimension of the Tibetan Plateau. "Plateau_3deg", "Plateau_6deg" and "Plateau_10deg" represent scenarios where the northern edge of the Plateau is extended northward by 3 degrees, 6 degrees, and 10 degrees, respectively. To generate topography files for these simulations, we first modify a global elevation dataset mapped onto the model grid ($0.9° \times 1.25°$), which is obtained from NCAR's supercomputer. We then use the NCAR Global Model Topography Generation Software (Lauritzen et al., 2015) to smooth the modified topography files.

Figure A1 shows the boundary topography in East Asia for these simulations. We take the "Plateau_3deg" run as an example to describe how we extended the northern edge of the Tibetan Plateau. We first target the region $35° - 55°N, 60° - 110°E$ (source region, hereafter), as highlighted by the black box in Fig. A1a. We then shift the elevation in this region northward by 3 degrees, replacing the elevation in the region $38° - 58°N, 60° - 110°E$ (the black box in Fig. A1b) with elevation of the source region. By doing so, we leave a topographic gap in the middle of the Plateau, as indicated

Accepted for publication in *Journal of Climate*. DOI 10.1175/JCLI-D-19-0319.1.

by the dashed box in Fig. A1b. We fill the gap with the elevation of today's Tibetan Plateau around that latitude. Figs. A1e-h present the vertical cross sections of modified elevation in the Plateau region.

The greenhouse gas (GHG) concentrations are set to default values as in the CESM preindustrial configuration (i.e., CO_2 is 284.7 ppm, CH_4 is 791.6 ppb, and N_2O is 275.68 ppb). The prescribed SST dataset is derived from the merged Hadley-OI SST and sea ice concentration (SIC) data set (Hurrell et al., 2008). Each experiment is integrated for 25 years, with the first 5 years discarded to avoid model drift; the climatology derived over the last 20 years is used for the analysis presented here.

For the idealized simulations (section 8), we use the F_IDEAL_PHYS component, i.e. the finite volume dynamical core of CAM5, which is based on the model described by Held and Suarez (1994). This idealized physics configuration is hemispheric and zonally symmetric, with neither a seasonal cycle nor land-sea contrast. It employs a Newtonian relaxation toward a prescribed zonal mean radiative equilibrium temperature profile to represent radiative cooling, with a relaxation time scale of 40 days. There is neither moisture nor diabatic heating in the dry dynamical core, which allows us to neglect the possible effects of the sensible heating and condensational heating on the atmospheric circulation. We introduce the Tibetan Plateau in the model by setting the surface geopotential in $25°N$ to $45°N, 65°E$ to $105°E$ to today's value. To obtain a relatively localized Plateau, elevation lower than 500m in the region is set to zero. We shift the Plateau meridionally to perturb relative positioning between westerlies and orography; by doing so, we mimic the seasonal migration of the westerly jet across the Plateau. We undertake five simulations, namely "Plateau", "PlateauN3", "PlateauN6",

Accepted for publication in *Journal of Climate*. DOI 10.1175/JCLI-D-19-0319.1.

248 "PlateauS3", and "PlateauS6". "Plateau" is the case where the Tibetan Plateau is fixed at
249 its present location, while the other cases represent scenarios where the Plateau is shifted
250 northward or southward by 3 or 6 degrees. Each simulation is integrated for 5 years, with
251 30 levels in the vertical, at a horizontal resolution of 0.9°×1.25° (same with the
252 "northward-extended Plateau" simulations). An initial spin-up period of 2 years is
253 discarded, leaving 3 years of data for analysis.

254 For the boundary orography in the CAM5, the resolved grid scale component is
255 the mean elevation in each grid box, i.e. the surface geopotential. The unresolved sub-
256 grid scale orography is parameterized as the turbulent mountain stress (TMS) and the
257 gravity wave drag (GWD) (Neale et al., 2010). In our simulations with both modified
258 resolved and modified sub-grid topography, the sub-grid scale variances needed for TMS
259 and GWD parameterizations were derived from the modified resolved topography (e.g.
260 Fig. A1) using the NCAR Global Model Topography Generation Software (Lauritzen et
261 al., 2015). Thus, the sub-grid scale variances are modified to be consistent with the
262 modified resolved topography.

263

264 **3. Termination of mei-yu in climatology**

265 In this section, we show that the mei-yu termination in observed climatology is
266 accompanied by the migration of core westerlies impinging on the Tibetan Plateau to the
267 north of $40°N$ and the disappearance of northerlies in northeastern China ($35° -$
268 $45°N, 110° - 120°E$).

269

270 ***a. Identification of the mei-yu termination in climatology***

Accepted for publication in *Journal of Climate*. DOI 10.1175/JCLI-D-19-0319.1.

Fig. 1g presents the temporal evolution of the climatological precipitation over eastern China ($110° - 120°E$), with dashed lines indicating timings of the rainfall stages derived from the SOMs analysis of the APHRODITE data (Fig. 1a). Fig. 1a shows the temporal extent of each of the five rainfall patterns illustrated in the remaining panels, i.e. "Spring" (pattern 1, Fig. 1b), "Pre-mei-yu" (pattern 2, Fig. 1c), "Mei-yu" (pattern 3, Fig. 1d), "Midsummer" (pattern 4, Fig. 1e), and "Fall" (pattern 5, Fig. 1f). Observational studies (Ding and Chan, 2005; Tao and Chen, 1987) suggest that the typical mei-yu season lasts from mid-June to mid-July. The SOMs-captured timing of the mei-yu spans the interval from June 23rd to July 20th, approximately matching this reported timing. For spatial patterns, the SOMs-derived mei-yu covers the Yangtze River valley ($27° - 34°N, 100° - 120°E$), which is consistent with the previously defined domain (Ding and Chan, 2005).

The mei-yu front is characterized by a strong meridional moisture gradient (Chen and Chang, 1980; Ding, 1992) and can be identified from sharp meridional gradients in equivalent potential temperature (θ_e) (Ninomiya, 1984, 2000; Ninomiya and Shibagaki, 2007). Figure 2 shows the meridional gradient of θ_e $\left(-\frac{\partial \theta_e}{\partial y}\right)$. Here, θ_e is approximately defined as $\theta_e = \theta + L_v q/c_p$ (Shaw and Pauluis, 2012), and the largest values of $-\frac{\partial \theta_e}{\partial y}$ indicate the location of the front. We interpret the latitudinal migration of the band of strong gradient to indicate the meridional movement of the frontal system. Fig. 2a presents the seasonal evolution of $-\frac{\partial \theta_e}{\partial y}$ over East China $(110° - 120°E)$ at 850mb. It shows that the maximum gradient, and hence the front, migrates northward during the mei-yu and disappears by midsummer. Vertical cross-sections further show weakening of

Accepted for publication in *Journal of Climate*. DOI 10.1175/JCLI-D-19-0319.1.

the front in central eastern China ($30° - 35°N, 110° - 120°E$) from mei-yu to midsummer (Figs. 2b-c). Figs. 2d-e depict the meridional moisture gradient and suggest that the moisture contrast over central eastern China weakens from mei-yu to midsummer.

Strong mid-tropospheric (500mb) ascending motion over central eastern China is also thought to be representative for the mei-yu season (Sampe and Xie, 2010). Fig. 3a shows the ascending motion at 500mb and suggests that our SOMs analysis accurately captured the mei-yu and midsummer stages. Both spatial distribution (Figs. 3b-c) and vertical cross sections (Figs. 3d-e) further indicate significant weakening of the ascending motion over central eastern China from mei-yu to midsummer.

b. Threshold latitude of jet for the mei-yu termination

Fig. 4a shows the seasonal migration of 200mb westerlies averaged over $80°E$ to $100°E$, where the '+' symbol indicates the latitude of maximum westerlies. Resembling model results from Kong et al (2017) but now from observational data, the mean jet axis over the Plateau is located at $40°N$ for most of the mei-yu season (Figure 4a); it then migrates a few degrees northwards during the transition from mei-yu to midsummer, and stays at $42°N$ or $43°N$ for most of midsummer before retreating southward in late August. Figs. 4b-e further depict the distinct shift of jet axis over the Plateau from $40°N$ in mei-yu to around $42°N$ in midsummer. It suggests that 40°N marks a latitudinal threshold for the termination of mei-yu.

c. Changes in orographic downstream northerlies from mei-yu to midsummer

Previous studies suggested the meridional wind plays an important role in the formation of the mei-yu (Chen and Bordoni, 2014; Park et al., 2012). Figs. 4f-j show variations of

Accepted for publication in *Journal of Climate*. DOI 10.1175/JCLI-D-19-0319.1.

mid-tropospheric meridional wind from mei-yu to midsummer. During the spring and pre-mei-yu stages, the extratropical northerlies are strong and converge with the tropical southerlies along $30°N$ over eastern China. The northerlies weaken and retreat to the north of $35°N$ during the mei-yu stage, while the southerlies become stronger and penetrate northward. During midsummer, the extratropical northerlies almost disappear, while the tropical southerlies penetrate to around $40°N$. Similar variation can be seen in the meridional winds at 700mb (not shown).

4. Termination of the mei-yu on interannual and synoptic timescales

In this section, we seek a more rigorous examination of the link between jet latitude, weakening of northerlies over northeastern China, and termination of the mei-yu on interannual and synoptic timescales.

a. Termination of the mei-yu on interannual timescales

The leading mode of summertime rainfall over East Asia exhibits a 'tripole' pattern with rainfall over northern and southern China varying out of phase with rainfall over central China (Hsu and Lin, 2007). Chiang et al (2017) identified the leading mode of interannual variability of East Asian summer rainfall over 1951-2007 by deriving an Empirical Orthogonal Function (EOF) from July-August APHRODITE rain gauge data (Fig. A2). They attributed one phase of the 'tripole' pattern – with wet northern and southern China and dry central China – to a significantly earlier termination of the mei-yu, accompanied by a shorter mei-yu duration and longer midsummer stage. They found

Accepted for publication in *Journal of Climate*. DOI 10.1175/JCLI-D-19-0319.1.

that the years with earlier mei-yu termination are associated with earlier northward migration of westerlies over the Tibetan Plateau.

Here, we examine the linkage between the jet positioning, strength of northerlies, and the mei-yu in the context of the interannual variation of mei-yu termination. We select anomalous high and low years based on the first principal component of Chiang et al. (2017) (Fig. A2b), but limited to 1979-2007, which is the time span of the ERA-Interim data we use. We identify 7 high years and 9 low years based on the principal component exceeding $+/-0.5$ standard deviation. For each group of years, we compute the daily climatological rainfall between April and September, and applied a 9-day running average. To find the corresponding rainfall stages, we assign the averaged rainfall for each day to a best-matching climatological SOMs rainfall pattern (Figs. 1b-f) based on the minimum Euclidean distance between each daily pattern and each of the SOMs patterns. Similar to Chiang et al. (2017), the matched timing for high and low years suggests the mei-yu in low years terminates three weeks later than in high years (Figs. 5a-b).

Hovmoller diagrams of the meridional gradient of θ_e (Figs. 5c-d) and mid-tropospheric ascending motion (Figs. 5e-f) suggest that the mei-yu stages identified by the SOMs analysis are reliable for both categories. Mei-yu stages of both high and low years are accompanied by sharp gradients of θ_e over central eastern China; and termination of the mei-yu is accompanied by weakening of the gradient of θ_e and northward migration of the maximum gradient to north of $35°N$, which is more evident in the lower years than the high years, though. Similarly, both high and low years exhibit

Accepted for publication in *Journal of Climate*. DOI 10.1175/JCLI-D-19-0319.1.

360 significant weakening of mid-tropospheric ascending motion over central eastern China
361 when mei-yu ends (Figs. 5e-f).

362 The associated behaviors of the jet latitude over the Plateau and northerlies over
363 eastern China for both composites are consistent with the climatology. The main feature
364 to note is that the jet axis remains at $40°N$ during the mei-yu stage for both high and low
365 years; this is despite the fact that the mei-yu stage has significantly longer duration in low
366 years compared to the high years. Prior to the mei-yu, the jet axis is south of $40°N$ in
367 both cases; after the mei-yu, the jet axis shifts north of $40°N$ (Figs. 5g-h). On the other
368 hand, a weakening and retreat of the northerlies, and increased northward penetration of
369 southerlies, appears at the transition from mei-yu to midsummer for both high and low
370 years (Figs. 5i-j). It is worth noting that the southward retreat of westerlies toward the
371 end of the summer monsoonal season is accompanied by a recurrence of northerlies in
372 northeastern China, suggesting a causal link between the jet axis position relative to
373 $40°N$ and the sign and strength of northerlies downstream of the Plateau.
374

375 ***b. Termination of the mei-yu on synoptic timescales***

376 Although the climatological westerlies exhibit a continuous northward migration from
377 spring to summer (Figs. 4a, Figs. 5g-h), on synoptic timescales the jet exhibits large and
378 rapid latitudinal excursions (Schiemann et al., 2009). This observation raises the question
379 of whether the connection between the jet position, strength of northerlies, and
380 occurrence of mei-yu-like regimes holds on synoptic timescales.

381 To test this, we assign each pentad from April 1st (pentad 19) to September 27th
382 (pentad 54) for each year over 1979 – 2007 (a total of 1044 pentads) to the best-matched

Accepted for publication in *Journal of Climate*. DOI 10.1175/JCLI-D-19-0319.1.

383 climatological SOMs rainfall pattern based on the minimum Euclidean distance. This
384 allows us to identify mei-yu-like pentads and to examine the associated circulations. In
385 contrast to the smooth climatological timing of each pattern (red lines in Fig. 6a), the
386 SOMs-matched patterns on the pentad basis from each year exhibit large variations (blue
387 lines in Fig. 6a). Fig. 6b shows the seasonal distribution of the assigned SOMs patterns of
388 the 1044 pentads. Specifically for the mei-yu pattern, Fig. 6b suggests that mei-yu-like
389 rainfall regimes could occur in spring or late summer, but are relatively rare at these
390 times. Mid-June to mid-July is the period when the mei-yu-like rain pattern most likely
391 occurs.

392 We now discuss distributions of the jet axis impinging on the Plateau (Fig. 6c)
393 and strength of meridional winds over northeastern China (Fig. 6d). On the pentad scale,
394 mei-yu-like patterns are most closely associated with jet axes ranging from $38°N$ to
395 $41°N$, while midsummer-like pentads are associated with jet axes between $40°N$ and
396 $43°N$. For the strength of the 500mb meridional wind over northeastern China, Fig. 6d
397 suggests that northerly winds (negative values) are strongest when the rainfall is spring-
398 like or pre-mei-yu-like; the northerlies tend to be weaker for mei-yu-like patterns. For
399 midsummer-like patterns, the 500mb meridional winds are both northerly and southerly,
400 with a preference for the latter. These findings suggest that the synoptic relationships
401 between the jet positions, the strength of northerlies and the rainfall stage are in general
402 agreement with the ones inferred from the climatology.

403 We now examine the question from the opposite perspective. If we classify all
404 1044 pentads based instead on their positioning of the jet axis over the Plateau, can we
405 see weaker orographic downstream northerlies and midsummer-like rain patterns during

Accepted for publication in *Journal of Climate*. DOI 10.1175/JCLI-D-19-0319.1.

406 pentads when the jet axis locates to the north of $40°N$, and vice versa? Figure 6e – which
407 shows the jet latitude between April-September for each year from 1979-2007 – indicates
408 that jet latitude exhibits large synoptic variability about the climatological migration
409 latitude (shown in red). There are overlaps in the jet latitudes between the mei-yu-like
410 pentads and the midsummer-like pentads when the jet latitude is associated with the
411 corresponding rainfall stage (Figure 6f; note that Fig. 6f is identical to Fig. 6c, although
412 they are generated based on different approaches), suggesting that the correlation
413 between the position of the jet and the mei-yu/midsummer regimes is not as tight as that
414 on climatological (Fig. 4) and interannual timescales (Fig. 5). Regardless, the close
415 synoptic relationship between the two is evident, namely that when the jet axis is between
416 $38°N$ and $41°N$, the corresponding rainfall patterns are mei-yu-like, while jet axes
417 occupying the interval bounded by $40°N$ and $43°N$ are midsummer-like. Likewise, when
418 the jet latitude is associated with the corresponding value of the 500mb meridional wind,
419 northeastern China more likely experiences northerlies when jet axes are south of $40°N$,
420 while southerlies more likely appear in the region when the jet is north of $40°N$ (Figure
421 6g).

422 Composites of pentads when the jet axis is located at $37°N$, $40°N$, and $43°N$ are
423 shown in Fig. 7. These composites confirm that the northerlies over northeastern China
424 significantly weaken as the jet migrates from positions over the Plateau to north of the
425 Plateau (Figs. 7a-f). The weakening of the meridional gradient of θ_e (Figs. 7g-i) and
426 ascending motion (not shown) are all paced with the weakening of the northerlies.
427 Finally, the pattern of rainfall extends northwards with a more northward mean jet axis
428 (Fig. 7j to Fig. 7l).

Accepted for publication in *Journal of Climate*. DOI 10.1175/JCLI-D-19-0319.1.

5. Connections between northerlies and mei-yu termination

In this section, we explore the dynamical connection between the disappearance of lower-to-mid tropospheric northerlies and the mei-yu termination.

a. General discussion

One view of how the northerlies maintain the mei-yu is that they advect cold, dry air southward, meeting with the warm, moist southerly flow and forming a steep moisture gradient over central China characteristic of the mei-yu front. The northerlies essentially disappear when mei-yu ends, leading to the demise of the strong moisture contrast (Figure 2). This view is in agreement with previous findings on the close connection between the mei-yu and cold air mass associated with northerlies (Li and Zhang, 2014; Seo et al., 2015; Tomita et al., 2011). Park et al. (2012) found that the mei-yu is associated with southward low moist static energy (MSE) flux (integrated from surface to 600mb) over northeastern China and northward high MSE flux over southeastern China. In this vein, the mei-yu terminates when the southward low MSE air disappears with northerlies. Chou and Neelin (2003) argued that advection of low MSE air over the northern reaches of monsoon regions limits the northward extent of summer monsoons, through the so-called 'ventilation' effect. In a similar vein, the advection of low MSE air by the northerly flow limits the northward extent of the rainfall over eastern China (Figs. 8a-c); as such, rainfall shifts to northeastern China in midsummer as the northerly flow retreats.

Accepted for publication in *Journal of Climate*. DOI 10.1175/JCLI-D-19-0319.1.

The northerlies are also crucial for the mei-yu formation through maintaining strong meridional wind convergence. Simulations with and without the Tibetan Plateau by Chen and Bordoni (2014) suggest that the presence of the Tibetan Plateau and the resultant orographic downstream meridional wind convergence is key to the formation of mei-yu. Figs. 8d-f show that meridional wind convergence over central eastern China is indeed considerably stronger in the mei-yu than in midsummer. It is worth noting that seasonal variation of meridional wind convergence over central eastern China (Fig. 8d) resembles the rainfall seasonality (Fig. 1g), indicating close connection between the two. As will be shown in the next section (5b), weakening of the meridional wind convergence dominates the reduction of moisture flux convergence associated with mei-yu termination.

b. Moisture budget analysis

We explicitly show the role of meridional wind anomalies on rainfall changes associated with mei-yu termination through a vertically-integrated moisture budget analysis. We follow Chen and Bordoni (2016) and employ moisture budget analysis to diagnose contributions to the moisture flux convergence. In long-term average, the moisture budget can be written as

$$\bar{P} - \bar{E} = -\overline{\langle \nabla \cdot (\vec{v} \cdot q) \rangle} \quad (1)$$

where P is precipitation, E is evaporation, $\vec{v}$ indicates horizontal winds, and q is specific humidity; $\overline{(\cdot)}$ indicates temporal mean, while $\langle \cdot \rangle$ indicates mass-weighted vertical integral from 1000 mb to 100 mb. Contribution to the vertically integrated moisture flux convergence by submonthly transient eddies is calculated from

Accepted for publication in *Journal of Climate*. DOI 10.1175/JCLI-D-19-0319.1.

$$trans = \overline{\langle \nabla \cdot (\vec{v} \cdot q) \rangle} - \langle \nabla \cdot (\bar{\vec{v}} \bar{q}) \rangle \quad (2)$$

Changes (δ) of vertically integrated moisture flux convergence between mei-yu and midsummer in climatology can be written as,

$$\delta(\bar{P} - \bar{E}) = -\delta\{\overline{\langle \nabla \cdot (\vec{v} \cdot q) \rangle}\} = -\delta\{\langle \nabla \cdot (\bar{\vec{v}} \bar{q}) \rangle\} - \delta(trans) \quad (3)$$

where δ indicates mei-yu minus midsummer. Equation (3) can be written as below by further decomposition of the term $-\delta\{\langle \nabla . (\bar{\vec{v}} \bar{q}) \rangle\}$,

$$-\delta\{\overline{\langle \nabla \cdot (\vec{v} \cdot q) \rangle}\} = -\langle \nabla \cdot (\overline{\vec{v}} \cdot \delta \bar{q}) \rangle - \langle \nabla \cdot (\delta \bar{\vec{v}} \cdot \bar{q}) \rangle - \langle \nabla \cdot (\delta \bar{\vec{v}} \cdot \delta \bar{q}) \rangle - \delta(trans) \quad (4)$$

(A) (B) (C) (D) (E)

where (A) indicates changes of vertically integrated moisture flux convergence, (B) is contribution by changes to the specific humidity, (C) is contribution by changes to the horizontal winds, (D) is contribution by changes to both specific humidity and horizontal winds, and (E) is contribution by submonthly transients. Note that variables without δ in (B) and (C) represent midsummer. Seager and Henderson (2013) noted that the divergence of the vertically integrated moisture transport does not balance the ERA-Interim P – E, possibly from the influence of the data assimilation. We find slight difference between the magnitude of $\delta(P - E)$ and (A), but the patterns between the two match well (not shown).

Figs. 9a-e shows terms (A) to (E) of equation (4), respectively, for the difference between the mei-yu and midsummer averages, in order to examine changes occurring to the components of the moisture flux budget between these intraseasonal stages. Not surprisingly, the mei-yu season exhibits enhanced moisture transport and moisture flux convergence over central eastern China (Fig. 9a). This enhancement is dominated by changes of horizontal winds (Fig. 9c), while the contribution by changes of specific

Accepted for publication in *Journal of Climate*. DOI 10.1175/JCLI-D-19-0319.1.

humidity is minimal (Fig. 9b). Contributions by the cross-perturbation term (Fig. 9d) and the submonthly transient eddies (Fig. 9e) are negligible. Decomposing contributions by the horizontal winds (Fig. 9c) to its zonal (Fig. 9f) and meridional components (Fig. 9g) indicates that changes in the meridional wind are essential to changes of the total moisture flux convergence. Contributions by the meridional winds could be further decomposed as following: $-\frac{\partial}{\partial y}(\delta v \cdot q) = -\left(\frac{\partial \delta v}{\partial y}\right) \cdot q - \delta v \cdot \frac{\partial q}{\partial y}$, where $-\left(\frac{\partial \delta v}{\partial y}\right) \cdot q$ is contribution by changes in meridional wind convergence, while $-\delta v \cdot \frac{\partial q}{\partial y}$ is contribution by changes in the meridional advection of moisture. Figs. 9h-i indicates that although both terms positively contribute to the moisture flux convergence, changes of meridional wind convergence play the dominant role.

We repeat the above analysis but in the context of the 'tripole mode' of East Asian rainfall interannual variability, using again the high and low year composites defined in section 4; we refer to changes (δ) as low years minus high years. We focus on the gap in the timings of mei-yu termination between high and low years, i.e. July 3rd to July 23rd. During this period, high years are already in the midsummer stage, while low years are still in mei-yu. The results (Fig. 10) show strong qualitative similarity to the analysis of Figure 9 for the difference between mei-yu and midsummer stages, and reinforce the conclusions drawn from Figure 9. Fig. 10a shows enhanced moisture flux convergence over central China in low years relative to high years. The resemblance between Figs. 10a, 10c, 10g and 10h highlights the crucial role of meridional wind convergence in changes of total moisture flux convergence during the period when high years are in midsummer while low years are still in mei-yu.

Accepted for publication in *Journal of Climate*. DOI 10.1175/JCLI-D-19-0319.1.

c. Relative contributions from northerlies and southerlies

The moisture budget analysis above clearly shows the central role of meridional wind changes in mei-yu termination. We have focused on the role of the extratropical northerlies, but one might argue that variations of the southerlies also contribute to the mei-yu termination. On average, southerlies over eastern China are indeed weaker in midsummer, although this weakening is mainly limited to south of $30°N$ (Figs. 4g-j). Fig. 9g also suggests the southerly moisture flux dominates contribution to the enhanced moisture flux convergence in mei-yu. However, the moisture budget analysis is diagnostic, so the southerlies can be, in part, interpreted as a feedback. In particular, diabatic heating from the mei-yu rainband and consequent vortex stretching will lead to a southerly flow because of Sverdrup vorticity balance (Rodwell and Hoskins, 2001). Furthermore, Fig. 4f shows that the most striking change in the meridional circulation associated with the mei-yu termination is disappearance of extratropical northerlies and northward penetration of southerlies. It suggests weakening in northerlies is the root cause of the transition from mei-yu to midsummer.

On shorter timescales, Fig. 10 suggests stronger and more persistent southward moisture flux, associated with enhanced northerlies, dominates the enhanced moisture flux convergence in low years during July 3rd to July 23rd. Further, our composites of meridional wind at pentads with different jet positions clearly show the weakening of extratropical northerlies when the jet is located north of the Plateau (Figs. 7d-f). However, there is no evident change in the strength of tropical southerlies among these composites.

Accepted for publication in *Journal of Climate*. DOI 10.1175/JCLI-D-19-0319.1.

We note in closing that relative roles of tropical southerlies and extratropical northerlies are still in debate. A recent idealized study by Son et al. (2019) suggests that orographic downstream southerlies are most crucial for the EASM. Tomita et al. (2011) and Suzuki and Hoskins (2009) suggest that the closing dates of baiu (the Japanese sector of the mei-yu-baiu rain belt) could be modified by the combined effects of both tropical and mid-latitude circulations.

6. Termination of the mei-yu with a northward-extended Tibetan Plateau

Based on the various lines of evidence presented in sections 3 to 5, we propose this hypothesis on the mei-yu termination: *the weakening and eventual disappearance of the northerlies over northeastern China leads to the demise of the mei-yu, and this weakening is a direct consequence of the northward shift of westerlies beyond the northern edge of the Plateau, around 40°N.* We speculate that the reduced orographic forcing on the westerlies during the northward jet transition causes the weakening of the orographic downstream northerlies

To test this hypothesis, we artificially perturb the orographic forcing of the Tibetan Plateau by changing the latitude of the northernmost edge of the Plateau in the Community Atmosphere Model version 5 (CAM5). The expectation here is that with a more northward-extended Plateau, mechanical forcing of the Plateau on the westerlies should strengthen; by our hypothesis, northerlies downstream of the Plateau should stay strong and mei-yu like conditions persist as a result.

Figs. 11a-d present the simulated seasonal evolution of 200mb zonal wind over the Plateau. With the presence of more northward-extended Plateau, the westerlies

Accepted for publication in *Journal of Climate*. DOI 10.1175/JCLI-D-19-0319.1.

565 impinging over the Plateau are able to migrate to higher latitude while the strength of the
566 westerlies becomes weaker. In agreement with observations (Fig. 4f), tropospheric
567 northerlies over northeastern China disappear from late June to late August in the
568 "Plateau_control" run (Fig. 11e). Note that the simulated disappearance of northerlies
569 occurs earlier (late June) than the observations (late July as suggested in Fig. 4f),
570 indicating some model bias. Our hypothesis predicts stronger and more persistent
571 northerlies downstream of the Plateau as orographic forcing strengthens. When the
572 Plateau extends northward by 3 degrees and 6 degrees, downstream northerlies indeed
573 persist longer, with the disappearance of northerlies occurring over a shorter time period
574 (Figs. 11f-g). When the Plateau extends northward by 10 degrees, northerlies prevail over
575 northeastern China throughout the summer season, though weakening of northerlies is
576 still notable from late June to August (Fig. 11h).

577 Given the intensified northerlies (Figs. 11e-h) and meridional convergence (not
578 shown), does the mei-yu front persist for longer duration in wider Plateau scenarios?
579 Note that due to the changed dimension of the Plateau, the geographic location of the
580 mei-yu in wider Plateau cases may differ from the typical mei-yu in the present day. We
581 thus identify the mei-yu front based on its expressed physical characteristics, i.e. sharp
582 meridional gradients in θ_e. Compared with the control run, the meridional gradient of θ_e
583 becomes stronger from April through June over central eastern China when the Plateau
584 extends northward by 6 degrees and 10 degrees (Figs. 11i-l). The relatively weak gradient
585 of θ_e in the "Plateau_3deg" case is consistent with disappearance of northerlies in mid-
586 late June (Figs. 11f,j). In July, southerlies occupy central to northeastern China in the
587 control run, while northerlies prevail over the region in the wider Plateau scenarios. As a

Accepted for publication in *Journal of Climate*. DOI 10.1175/JCLI-D-19-0319.1.

588 result, Figs. 11i-l show that the July meridional gradient of θ_e is more pronounced over
589 northeastern China $(40-45°N, 110°-120°E)$ in the wider Plateau scenarios than in
590 the control run. This suggests that the wider Plateau cases are able to maintain the mei-
591 yu-like front over northeastern China in July.

592 Additionally, summer rainfall over East Asia could be partitioned into "banded",
593 which is associated with large-scale frontal convergence, and "local", which is possibly
594 driven by local buoyancy or topography (Day et al., 2018). Day et al. (2018) suggests that
595 "banded" rainfall constitutes the majority of precipitation during pre-mei-yu and mei-yu,
596 while midsummer is mainly characterized by sporadic "local" rainfall. We view the
597 existence of banded large-scale rainfall as an indicator of mei-yu-like rainfall. Therefore,
598 we expect more pronounced mei-yu-like rain bands over northeastern China in July in the
599 wider Plateau simulations. To estimate the amount of banded rainfall, we examine the
600 large-scale rainfall from the model output[Ψ]. When northerlies over northeastern China
601 are stronger and more persistent, large-scale rainfall over eastern China should be
602 intensified as well. Figs. 11m-p and Figs. 11q-t show the spatial distribution of large-
603 scale rainfall in June and July, respectively. The leftmost panel suggests that the banded
604 structure of rainfall in the control run is pronounced in June but disappears in July. In
605 contrast, the rain bands remain in wider Plateau cases in July, though with weaker
606 magnitude and more northward location.

607 One caveat to the "northward extended Plateau" simulations is that it is difficult
608 to exclude the potential role of diabatic heating over the Plateau on the changes in the

[Ψ] Here, large-scale rainfall is rainfall from large-scale circulation that can be resolved by the model resolution, while convective rainfall is parameterized based on the Zhang-McFarlane scheme (Zhang and McFarlane, 1995).

Accepted for publication in *Journal of Climate*. DOI 10.1175/JCLI-D-19-0319.1.

609 circulation and rainfall over East Asia (e.g. Li and Yanai, 1996; Wu et al., 2012). Future
610 studies are required to fully understand the relative contribution of the mechanical and
611 thermal forcing of the Tibetan Plateau on the evolution of the EASM.
612
613 **7. Response of downstream northerlies to the positioning of the jet in a dry**
614 **dynamical core simulation**
615 In this section, we use the dry dynamical core from CAM5 to further show that the
616 downstream northerlies can originate from mechanical forcing on the westerlies by the
617 Tibetan Plateau, and that the northerlies disappear when the westerlies impinging on the
618 Plateau shift sufficiently northward of it. The idealized physics of the dry dynamical core
619 (see section 2d) allow us to neglect possible effects of moisture feedbacks and diabatic
620 heating on the westerlies. We relax the model to the same equilibrium radiative
621 temperature profile in all cases, and perturb the relative positioning between westerlies
622 and the Plateau by shifting the Plateau meridionally in order to mimic the northward
623 seasonal migration of the westerlies.
624
625 ***a. Results***
626 Figure 12 shows the zonal winds and meridional winds from the idealized simulations.
627 When the Plateau is shifted northward by 6 degrees ("PlateauN6"; Figs. 12a, k), the
628 configuration of westerlies around the Plateau resembles spring in observations, with a
629 much stronger southern branch of westerly wind to the south of the Plateau compared
630 with its counterpart to the North. In contrast to "PlateauN6", the southern branch of
631 westerlies in the "PlateauN3" scenario is weaker, while the northern branch is stronger

Accepted for publication in *Journal of Climate*. DOI 10.1175/JCLI-D-19-0319.1.

(Figs. 12b, l). The northern branch becomes further pronounced when the Plateau is at the modern day location (Figs. 12c, m). The westerlies are well north of the topography when the Plateau is shifted to the south (Figs. 12d-e, n-o). In short, these scenarios mimic the northward seasonal migration of westerlies relative to the Tibetan Plateau from spring to summer. The responses of orographic downstream northerlies to perturbations of relative positioning between westerlies and the Plateau are not clear-cut monotonic (Figs. 12f-j; Figs. 12p-t). However, the simulations demonstrate that the orographic downstream northerlies exhibit general weakening as location of westerlies changes from south of the Plateau to north (Figs. 12 f-j, p-t). It is also worth noting that the downstream southerlies strengthen as the core of the westerlies shift from being south of the Plateau to north of it (Figs. 12 f-j, p-t).

b. Mechanism revealed in the dry dynamical core simulations

The low eddy geopotential height anomaly at 500mb to the east of the orography appears to be a dynamical consequence of the orographic forcing on the atmosphere (Bolin, 1950; Charney and Eliassen, 1949; Held, 1983) (the eddy geopotential height is defined as the geopotential height with the global zonal mean of geopotential height subtracted). We use the variation of eddy geopotential height at 500mb downstream of the Plateau as an indicator of changes in orographically forced stationary waves. In our idealized simulations, "Plateau" to "PlateauS6" are the closest analogues to the seasonal shift of the jet to the north of $40°N$ in the real world, showing a weakening of orographic downstream northerlies from the former to the latter (Figure 12). We show the eddy geopotential height at 500mb from these simulations in Figs. 13a-c. Weakening of the

Accepted for publication in *Journal of Climate*. DOI 10.1175/JCLI-D-19-0319.1.

orographic downstream cyclonic circulation from "Plateau" to "PlateauS6" is evident, suggesting that the weakening of the mechanical forcing by the Plateau as the jet shifts northward is the primary cause of the weakening of northerlies.

Lutsko and Held (2016) examined the transition from zonal to meridional propagation of orographically induced stationary waves by varying the height of the orography. They found that the stationary wave response is meridionally trapped, zonally propagating for weaker orographic forcing (i.e. lower orography altitude). When the forcing is increased, the wave propagates more meridionally and more into the tropics. We find similar behavior in our simulations. When the westerlies are impinging on the Plateau, the orographic downstream stationary waves propagate equatorward. As the Plateau is moved to the South, the orographic forcing weakens and the propagation of the stationary waves becomes more zonal. Figs. 13d-f present the quasi-geostrophic eddy streamfunction and the horizontal Eliassen-Palm (EP) flux (Plumb, 1985; equation 5.7) at 250mb. Following Lutsko and Held (2016), we show the ratio of the meridional component to the zonal component of the EP flux at 250mb averaged in $25° - 45°N, 100° - 150°E$ (highlighted with green dashed lines in Figs. 13d-f) in Fig. 13g. As positioning of the westerlies changes from south of the Plateau to the north, the direction of the horizontal wave propagation downstream of the Plateau becomes more zonal, and the eddy streamfunction weakens (Figs. 13d-f), further indicating reduced orographic forcing as the jet shifts to north of the Plateau.

Taken together, when the westerlies shift to the north of the Plateau, orographic forcing on the westerlies weakens, leading to reduced cyclonic circulation downstream of

Accepted for publication in *Journal of Climate*. DOI 10.1175/JCLI-D-19-0319.1.

677 the Plateau. Weakening of the cyclonic circulation in turn weakens the northerlies
678 downstream of the topography.

679 ***c. Weakening of the downstream cyclonic circulation in observations***

680 We discuss to what extent the mechanism revealed in the dry dynamical core simulations
681 is seen in the observed mei-yu termination. Resembling the dry dynamical core runs
682 (Figs. 13a-c), Figure 14 shows weakening of the cyclonic circulation over northeastern
683 China from mei-yu to midsummer. Figure 15 shows hovmoller diagrams of eddy
684 geopotential height (Z') at 200mb and 500mb averaged over $110°E\ to\ 150°E$ (denoted
685 by dashed lines in Figure 14) for climatology of 1979-2007 (Figs. 15a,d), and for
686 composites of high years (Figs. 15b, e) and low years (Figs. 15c, f) over 1979-2007.
687 Here, the high and low years are selected based on the PC1 of July-August rainfall over
688 East Asia (Chiang et al., 2017) (see section 4). The eddy geopotential height at 200mb
689 changes from negative values to positive values during mei-yu termination in all three
690 cases, and indicates a transition from cyclonic to anticyclonic circulation in the upper
691 troposphere (Figs. 15a-c). The anticyclonic circulation exists throughout the midsummer
692 stage, and reverts back to a cyclonic circulation when midsummer ends. In agreement
693 with Figure 14, the eddy geopotential height at 500mb also represents an abrupt
694 weakening of the cyclonic circulation (Figs. 15d-f). These results support our
695 interpretation that weakening of the tropospheric cyclonic circulation leads to
696 disappearance of the northerlies.
697
698
699

Accepted for publication in *Journal of Climate*. DOI 10.1175/JCLI-D-19-0319.1.

8. Summary

This study investigates how changes in the meridional position of the westerly jet impinging over the Tibetan Plateau affects termination of the mei-yu stage of the East Asian summer monsoon. Specifically, we ask whether there is a threshold in terms of the jet latitude over the Tibetan Plateau that controls the mei-yu termination.

In agreement with Kong et al. (2017) and Molnar et al. (2010), we show that the mei-yu termination in the climatology is accompanied by the northward migration of the jet axis away from the northern edge of the Tibetan Plateau at $40°N$. Concurrently, tropospheric northerlies over northeastern China weaken during the mei-yu and disappear when the mei-yu ends. Further examinations suggest that the close linkage between transit of jet axis beyond the northern edge of the Plateau, weakening of downstream northerlies, and mei-yu termination also holds on interannual timescales. As westerlies exhibit large meridional excursions on synoptic timescales, we then examine whether the above connection holds on shorter (i.e. pentad) timescales. We found that the jet axis ranges between $38°N$ to $41°N$ for mei-yu-like pentads, while midsummer-like pentads are associated with the jet axis between $40°N$ to $43°N$. Furthermore, northeastern China $(110° - 120°E, 35° - 40°N)$ exhibits strong northerly wind during mei-yu-like pentads, while the northerly wind almost disappears among midsummer-like pentads.

We argue that the reduction of the northerlies is causally linked to the demise of mei-yu through the following processes. Firstly, reduction of the northerlies leads to weakening of the meridional contrast of equivalent potential temperature over central China, which is crucial for the maintenance of the mei-yu front (Li and Lu, 2017; Park et al., 2012). Furthermore, invoking the "ventilation effect" (Chou and Neelin, 2003), strong

Accepted for publication in *Journal of Climate*. DOI 10.1175/JCLI-D-19-0319.1.

northerlies over northern China during mei-yu limit the northward extension of the rain band by southward advection of low MSE air; when northerlies disappear, the "ventilation effect" is gone and rainfall extends to northeastern China in midsummer. Lastly, disappearance of northerlies weakens the meridional wind convergence. Moisture budget analyses show that the significant reduction of total moisture flux convergence over central eastern China from mei-yu to midsummer is mainly due to weakening of meridional wind convergence.

We argue that weakening of orographic downstream northerlies is caused by reduced orographic forcing on the westerlies as the jet migrates beyond the Plateau. To test this, we perform idealized simulations with CAM5 where the northern edge of the Plateau is artificially extended northwards, the idea being that orographic forcing should strengthen and thus the mei-yu should terminate later in such cases. The simulated results support our predictions. With the northern edge of the Plateau extended northward, northerlies become more persistent, stronger, and the mei-yu-like (i.e. banded) rainfall regime becomes more pronounced over northeastern China. Several paleoclimate studies suggest that the uplift of the northern Tibetan Plateau intensifies the EASM (Baldwin and Vecchi, 2016; Tang et al., 2013; Zhang et al., 2012), which is qualitatively consistent with results from our wider Plateau simulations. However, the mechanisms proposed by these studies are different from ours. Zhang et al. (2012) links the intensification of the EASM to westward extension of the western Pacific subtropical high with the uplift of the northern Tibetan Plateau, while Tang et al. (2013) and Baldwin and Vecchi (2016) invoke the thermal effect of the northern Plateau on the EASM. Further studies are

Accepted for publication in *Journal of Climate*. DOI 10.1175/JCLI-D-19-0319.1.

745 needed to elucidate how changes in the mechanical forcing of the Plateau have
746 contributed to the past evolution of the EASM.

747 To further explore the mechanical origins of the downstream circulation response
748 to Plateau topography, we employ a dry dynamical core with a Plateau-like feature
749 embedded in the core of the simulated westerlies. We artificially perturb the relative
750 positioning between westerlies and the Plateau by shifting the Plateau meridionally.
751 Similar to observations, we found that the orographic downstream northerlies weaken as
752 positioning of the jet relative to the Plateau changes from south to north. These
753 simulations highlight the importance of the mechanistic influence of the Tibetan Plateau
754 on the downstream northerlies and hence on the termination of the mei-yu. This is in
755 agreement with the results of Takahashi and Battisti (2007) (see Figure 7 of Molnar et al.
756 (2010)). They successfully simulated a mei-yu-like front in an aquaplanet configuration
757 that excludes the land-ocean thermal contrast and retains the mechanical interplay
758 between the westerly jet and the Tibetan Plateau. We interpret the weakening of the
759 orographic downstream northerlies to reflect changes in the orographically forced
760 stationary waves. As westerlies migrate beyond the Plateau, the cyclonic circulation to
761 the east of the Plateau weakens. Additional diagnostics show that the quasi-geostrophic
762 eddy streamfunction is reduced and the propagation of the orographic downstream
763 stationary waves becomes more zonal. These results suggest weakening of the orographic
764 forcing on the westerlies when the westerlies are north of the Plateau. Finally, we
765 examine the observational data to see if the mechanisms inferred from the idealized
766 simulations occur in the observed mei-yu termination. We find that mei-yu termination is

Accepted for publication in *Journal of Climate*. DOI 10.1175/JCLI-D-19-0319.1.

767 indeed accompanied by a weakening of the cyclonic circulation at 500mb downstream of
768 the Plateau, indicating weakening of the orographic forcing.

769 In short, the above findings suggest that the northern edge of the Tibetan Plateau
770 at 40°N acts as a latitudinal threshold for jet position that triggers the termination of the
771 mei-yu. The northerlies over northeastern China disappear as the jet axis over the Plateau
772 migrates north of $40°N$, and which in turn shuts off the meridional circulation
773 maintaining the mei-yu front and terminates the mei-yu. This view supports the
774 speculation by Molnar et al. (2010), who argues the crucial role of the mechanical effects
775 of the Tibetan Plateau on the modulation of mei-yu.

776 Fundamental questions remain. Here we have only considered the role of the
777 meridional position of the westerlies impinging over the Plateau on the termination of the
778 mei-yu. Though the results appear to support our speculation that $40°N$ is the threshold
779 of jet latitude that terminates the mei-yu, other characteristics of the westerlies could play
780 a role. Recent studies have proposed connections between rainfall over the Yangtze River
781 Basin with various characteristics of westerlies, such as the zonal variation of the jet
782 center (Xie et al., 2015), the intensity of the jet (Wang and Zuo, 2016), and different
783 configurations of the subtropical jet and polar front jet (Huang et al., 2014; Li and Zhang,
784 2014). Additionally, though this study focuses on the role of the mechanical interaction
785 between the westerlies and the Tibetan Plateau on the termination of mei-yu, we cannot
786 yet exclude other interpretations such as the influence of mid-tropospheric warm
787 advection (Kosaka et al., 2011; Kuwano-Yoshida et al., 2013; Sampe and Xie, 2010) and
788 the role of surface heating over the Tibetan Plateau on East Asian summer rainfall (Wang
789 et al., 2008; Yanai and Wu, 2006). Finally, role of the adjacent ocean on the mei-yu

Accepted for publication in *Journal of Climate*. DOI 10.1175/JCLI-D-19-0319.1.

merits further investigations. Recent studies suggest that variation of sea surface temperature over the East China Sea to the northwestern Pacific affect seasonal migration (Gan et al., 2019) and intensity (Kuwano-Yoshida et al., 2013) of the mei-yu-baiu rainband.

Acknowledgements

This work was supported by the National Science Foundation Grant AGS-1405479. The simulations in this study were conducted on the Yellowstone high-performance IBM cluster at NCAR. We thank Dr. Hisashi Nakamura and three anonymous reviewers for their careful reviews and insightful comments. We thank Leif M. Swenson for sharing codes of the SOMs; and Dr. Michael J. Herman for helpful discussions and for his constructive comments and edits on an earlier draft of this paper. WK thanks Dr. Peter H. Lauritzen for his help in the use of the NCAR Global Model Topography Generation Software. APHRODITE precipitation data were obtained from http://www.chikyu.ac.jp/precip/index.html, and we acknowledge the ECMWF for making the ERA-Interim data publicly available (http://apps.ecmwf.int/datasets/data/interim-full-moda/). Boundary topography and model output for the extended Plateau simulations and the dry dynamical core simulations are archived and available at https://datadryad.org/stash/dataset/doi:10.6078/D1ZH51. Code for calculations of the three dimensional Eliassen-Palm flux is obtained from http://www.atmos.rcast.u-tokyo.ac.jp/nishii/programs/index.html. Calculation and visualizations are based on the National Center for Atmospheric Research Command Language (NCL) (version 6.4.0)

Accepted for publication in *Journal of Climate*. DOI 10.1175/JCLI-D-19-0319.1.

812 [Software]. (2017). Boulder, Colorado: UCAR/NCAR/CISL/TDD.

813 http://dx.doi.org/10.5065/D6WD3XH5.

814

815 **Appendix**

816 Figure A1 here

817 Figure A2 here

818 **References**

819 Baldwin, J., and Vecchi, G. (2016). Influence of the Tian Shan on Arid Extratropical
820 Asia. J. Clim. *29*, 5741–5762.

821 Bolin, B. (1950). On the Influence of the Earth's Orography on the General Character
822 of the Westerlies. Tellus *2*, 184–195.

823 Broccoli, A.J., and Manabe, S. (1992). The Effects of Orography on Midlatitude
824 Northern Hemisphere Dry Climates. J. Clim. *5*, 1181–1201.

825 Chang, C.-H., and Johnson, N.C. (2015). The continuum of wintertime Southern
826 Hemisphere atmospheric teleconnection patterns. J. Clim.

827 Charney, J.G., and Eliassen, A. (1949). A Numerical Method for Predicting the
828 Perturbations of the Middle Latitude Westerlies. Tellus *1*, 38–54.

829 Chattopadhyay, R., Sahai, A.K., and Goswami, B.N. (2008). Objective Identification of
830 Nonlinear Convectively Coupled Phases of Monsoon Intraseasonal Oscillation:
831 Implications for Prediction. J. Atmospheric Sci. *65*, 1549–1569.

832 Chen, J., and Bordoni, S. (2014). Orographic Effects of the Tibetan Plateau on the
833 East Asian Summer Monsoon: An Energetic Perspective. J. Clim. *27*, 3052–3072.

834 Chen, J., and Bordoni, S. (2016). Early Summer Response of the East Asian Summer
835 Monsoon to Atmospheric CO2 Forcing and Subsequent Sea Surface Warming. J. Clim.
836 *29*, 5431–5446.

837 Chen, T.-J.G., and Chang, C.-P. (1980). The Structure and Vorticity Budget of an Early
838 Summer Monsoon Trough (Mei-Yu) over Southeastern China and Japan. Mon.
839 Weather Rev. *108*, 942–953.

840 Chiang, J.C.H., Fung, I.Y., Wu, C.-H., Cai, Y., Edman, J.P., Liu, Y., Day, J.A., Bhattacharya,
841 T., Mondal, Y., and Labrousse, C.A. (2015). Role of seasonal transitions and westerly
842 jets in East Asian paleoclimate. Quat. Sci. Rev. *108*, 111–129.

Accepted for publication in *Journal of Climate*. DOI 10.1175/JCLI-D-19-0319.1.

843 Chiang, J.C.H., Swenson, L.M., and Kong, W. (2017). Role of seasonal transitions and
844 the westerlies in the interannual variability of the East Asian summer monsoon
845 precipitation. Geophys. Res. Lett. *44*, 2017GL072739.

846 Chou, C., and Neelin, J.D. (2003). Mechanisms Limiting the Northward Extent of the
847 Northern Summer Monsoons over North America, Asia, and Africa. J. Clim. *16*, 406–
848 425.

849 Chu, J.-E., Hameed, S.N., and Ha, K.-J. (2012). Nonlinear, Intraseasonal Phases of the
850 East Asian Summer Monsoon: Extraction and Analysis Using Self-Organizing Maps. J.
851 Clim. *25*, 6975–6988.

852 Cook, K.H., and Held, I.M. (1992). The Stationary Response to Large-Scale Orography
853 in a General Circulation Model and a Linear Model. J. Atmospheric Sci. *49*, 525–539.

854 Day, J.A., Fung, I., and Liu, W. (2018). Changing character of rainfall in eastern China,
855 1951–2007. Proc. Natl. Acad. Sci. 201715386.

856 Dee, D.P., Uppala, S.M., Simmons, A.J., Berrisford, P., Poli, P., Kobayashi, S., Andrae, U.,
857 Balmaseda, M.A., Balsamo, G., Bauer, P., et al. (2011). The ERA-Interim reanalysis:
858 configuration and performance of the data assimilation system. Q. J. R. Meteorol. Soc.
859 *137*, 553–597.

860 Ding, Y. (1992). Summer Monsoon Rainfalls in China. J. Meteorol. Soc. Jpn. Ser II *70*,
861 373–396.

862 Ding, Y., and Chan, J.C.L. (2005). The East Asian summer monsoon: an overview.
863 Meteorol. Atmospheric Phys. *89*, 117–142.

864 Enomoto, T., Hoskins, B.J., and Matsuda, Y. (2003). The formation mechanism of the
865 Bonin high in August. Q. J. R. Meteorol. Soc. *129*, 157–178.

866 Flohn, H. (1957). Large-scale aspects of the “summer monsoon” in South and East
867 Asia. J Meteor Soc Jpn. *75*, 180–186.

868 Gan, B., Kwon, Y.-O., Joyce, T.M., Chen, K., and Wu, L. (2019). Influence of the
869 Kuroshio Interannual Variability on the Summertime Precipitation over the East
870 China Sea and Adjacent Area. J. Clim. *32*, 2185–2205.

871 Hahn, D.G., and Manabe, S. (1975). The Role of Mountains in the South Asian
872 Monsoon Circulation. J. Atmospheric Sci. *32*, 1515–1541.

873 Held, I.M. (1983). Stationary and quasi-stationary eddies in the extratropical
874 troposphere: Theory. Large-Scale Dynamical Processes in The Atmosphere. In
875 Large-Scale Dynamic Processes in the Atmosphere, pp. 127–168.

Accepted for publication in *Journal of Climate*. DOI 10.1175/JCLI-D-19-0319.1.

876 Held, I.M., and Suarez, M.J. (1994). A Proposal for the Intercomparison of the
877 Dynamical Cores of Atmospheric General Circulation Models. Bull. Am. Meteorol.
878 Soc. *75*, 1825–1830.

879 Hong, X., and Lu, R. (2016). The Meridional Displacement of the Summer Asian Jet,
880 Silk Road Pattern, and Tropical SST Anomalies. J. Clim. *29*, 3753–3766.

881 Hong, X., Lu, R., and Li, S. (2017). Asymmetric Relationship between the Meridional
882 Displacement of the Asian Westerly Jet and the Silk Road Pattern. Adv. Atmospheric
883 Sci.

884 Hoskins, B.J., and Karoly, D.J. (1981). The Steady Linear Response of a Spherical
885 Atmosphere to Thermal and Orographic Forcing. J. Atmospheric Sci. *38*, 1179–1196.

886 Hsu, H.-H., and Lin, S.-M. (2007). Asymmetry of the Tripole Rainfall Pattern during
887 the East Asian Summer. J. Clim. *20*, 4443–4458.

888 Huang, D.-Q., Zhu, J., Zhang, Y.-C., and Huang, A.-N. (2014). The Different
889 Configurations of the East Asian Polar Front Jet and Subtropical Jet and the
890 Associated Rainfall Anomalies over Eastern China in Summer. J. Clim. *27*, 8205–
891 8220.

892 Hurrell, J.W., Hack, J.J., Shea, D., Caron, J.M., and Rosinski, J. (2008). A New Sea
893 Surface Temperature and Sea Ice Boundary Dataset for the Community Atmosphere
894 Model. J. Clim. *21*, 5145–5153.

895 Hurrell, J.W., Holland, M.M., Gent, P.R., Ghan, S., Kay, J.E., Kushner, P.J., Lamarque, J.-
896 F., Large, W.G., Lawrence, D., Lindsay, K., et al. (2013). The Community Earth System
897 Model: A Framework for Collaborative Research. Bull. Am. Meteorol. Soc. *94*, 1339–
898 1360.

899 Johnson, N.C. (2013). How Many ENSO Flavors Can We Distinguish?*. J. Clim. *26*,
900 4816–4827.

901 Johnson, N.C., Feldstein, S.B., and Tremblay, B. (2008). The Continuum of Northern
902 Hemisphere Teleconnection Patterns and a Description of the NAO Shift with the
903 Use of Self-Organizing Maps. J. Clim. *21*, 6354–6371.

904 Kitoh, A. (2004). Effects of Mountain Uplift on East Asian Summer Climate
905 Investigated by a Coupled Atmosphere–Ocean GCM. J. Clim. *17*, 783–802.

906 Kohonen, T. (2001). Self-Organizing Maps (Springer).

907 Kohonen, T., Hynninen, J., Kangas, J., and Laaksonen, J. (1996). SOM_PAK: The self-
908 organizing maps program package. (Helsinki University of Technology, Faculty of
909 Information Technology, Laboratory of Computer and Information Science).

Accepted for publication in *Journal of Climate*. DOI 10.1175/JCLI-D-19-0319.1.

910 Kong, W., Swenson, L.M., and Chiang, J.C.H. (2017). Seasonal Transitions and the
911 Westerly Jet in the Holocene East Asian Summer Monsoon. J. Clim. *30*, 3343–3365.

912 Kosaka, Y., Xie, S.-P., and Nakamura, H. (2011). Dynamics of Interannual Variability
913 in Summer Precipitation over East Asia. J. Clim. *24*, 5435–5453.

914 Kuwano-Yoshida, A., Taguchi, B., and Xie, S.-P. (2013). Baiu Rainband Termination in
915 Atmospheric and Coupled Atmosphere–Ocean Models. J. Clim. *26*, 10111–10124.

916 Lauritzen, P.H., Bacmeister, J.T., Callaghan, P.F., and Taylor, M.A. (2015). NCAR global
917 model topography generation software for unstructured grids. Geosci. Model Dev.
918 Discuss. *8*, 4623–4651.

919 Li, C., and Yanai, M. (1996). The Onset and Interannual Variability of the Asian
920 Summer Monsoon in Relation to Land–Sea Thermal Contrast. J. Clim. *9*, 358–375.

921 Li, L., and Zhang, Y. (2014). Effects of Different Configurations of the East Asian
922 Subtropical and Polar Front Jets on Precipitation during the Mei-Yu Season. J. Clim.
923 *27*, 6660–6672.

924 Li, X., and Lu, R. (2017). Extratropical Factors Affecting the Variability in Summer
925 Precipitation over the Yangtze River Basin, China. J. Clim. *30*, 8357–8374.

926 Liang, X.-Z., and Wang, W.-C. (1998). Associations between China monsoon rainfall
927 and tropospheric jets. Q. J. R. Meteorol. Soc. *124*, 2597–2623.

928 Lutsko, N.J., and Held, I.M. (2016). The Response of an Idealized Atmosphere to
929 Orographic Forcing: Zonal versus Meridional Propagation. J. Atmospheric Sci. *73*,
930 3701–3718.

931 Manabe, S., and Terpstra, T.B. (1974). The Effects of Mountains on the General
932 Circulation of the Atmosphere as Identified by Numerical Experiments. J.
933 Atmospheric Sci. *31*, 3–42.

934 Molnar, P., Boos, W.R., and Battisti, D.S. (2010). Orographic Controls on Climate and
935 Paleoclimate of Asia: Thermal and Mechanical Roles for the Tibetan Plateau. Annu.
936 Rev. Earth Planet. Sci. *38*, 77–102.

937 Murakami, T. (1951). On the Study of the Change of the Upper Westerlies in the Last
938 Stage of Baiu Season (Rainy Season in Japan). J. Meteorol. Soc. Jpn. Ser II *29*, 162–
939 175.

940 Neale, R.B., Gettelman, A., Park, S., Conley, A.J., Kinnison, D., Marsh, D., Smith, A.K.,
941 Vitt, F., Morrison, H., Cameron-smith, P., et al. (2010). Description of the NCAR
942 Community Atmosphere Model (CAM 5.0), Tech. Note NCAR/TN-486+STR, Natl.
943 Cent. for Atmos. In 6of7 ZHAO ET AL.: AEROSOL FIE SIMULATED BY CAMS L08806,
944 pp. 2009–038451.

Accepted for publication in *Journal of Climate*. DOI 10.1175/JCLI-D-19-0319.1.

945 Ninomiya, K. (1984). Characteristics of Baiu front as a predominant subtropical
946 front in the summer northern hemisphere. J. Meteorol. Soc. Jpn. *62*, 880–894.

947 Ninomiya, K. (2000). Large- and Meso-α-scale Characteristics of Meiyu/Baiu Front
948 Associated with Intense Rainfalls in 1-10 July 1991. J. Meteorol. Soc. Jpn. Ser II *78*,
949 141–157.

950 Ninomiya, K., and Shibagaki, Y. (2007). Multi-Scale Features of the Meiyu-Baiu Front
951 and Associated Precipitation Systems. J. Meteorol. Soc. Jpn. Ser II *85B*, 103–122.

952 Park, H.-S., Chiang, J.C.H., and Bordoni, S. (2012). The Mechanical Impact of the
953 Tibetan Plateau on the Seasonal Evolution of the South Asian Monsoon. J. Clim. *25*,
954 2394–2407.

955 Plumb, R.A. (1985). On the Three-Dimensional Propagation of Stationary Waves. J.
956 Atmospheric Sci. *42*, 217–229.

957 Rodwell, M.J., and Hoskins, B.J. (2001). Subtropical Anticyclones and Summer
958 Monsoons. J. Clim. *14*, 3192–3211.

959 Sampe, T., and Xie, S.-P. (2010). Large-Scale Dynamics of the Meiyu-Baiu Rainband:
960 Environmental Forcing by the Westerly Jet*. J. Clim. *23*, 113–134.

961 Schiemann, R., Lüthi, D., and Schär, C. (2009). Seasonality and Interannual
962 Variability of the Westerly Jet in the Tibetan Plateau Region*. J. Clim. *22*, 2940–2957.

963 Seager, R., and Henderson, N. (2013). Diagnostic Computation of Moisture Budgets
964 in the ERA-Interim Reanalysis with Reference to Analysis of CMIP-Archived
965 Atmospheric Model Data. J. Clim. *26*, 7876–7901.

966 Seo, K.-H., Son, J.-H., Lee, J.-Y., and Park, H.-S. (2015). Northern East Asian Monsoon
967 Precipitation Revealed by Airmass Variability and Its Prediction. J. Clim. *28*, 6221–
968 6233.

969 Shaw, T.A., and Pauluis, O. (2012). Tropical and Subtropical Meridional Latent Heat
970 Transports by Disturbances to the Zonal Mean and Their Role in the General
971 Circulation. J. Atmospheric Sci. *69*, 1872–1889.

972 Son, J.-H., Seo, K.-H., and Wang, B. (2019). Dynamical Control of the Tibetan Plateau
973 on the East Asian Summer Monsoon. Geophys. Res. Lett. *0*.

974 Staff Members of the Section of Synoptic and Dynamic Meteorology, I. of G. and M.,
975 Academia Sinica, Peking (1958). On the General Circulation over Eastern Asia (II).
976 Tellus *10*, 58–75.

Accepted for publication in *Journal of Climate*. DOI 10.1175/JCLI-D-19-0319.1.

977 Suzuki, S., and Hoskins, B. (2009). The Large-Scale Circulation Change at the End of
978 the Baiu Season in Japan as Seen in ERA40 Data. J. Meteorol. Soc. Jpn. - J METEOROL
979 SOC JPN *87*, 83–99.

980 Takahashi, K., and Battisti, D.S. (2007). Processes Controlling the Mean Tropical
981 Pacific Precipitation Pattern. Part I: The Andes and the Eastern Pacific ITCZ. J. Clim.
982 *20*, 3434–3451.

983 Tang, H., Micheels, A., Eronen, J.T., Ahrens, B., and Fortelius, M. (2013).
984 Asynchronous responses of East Asian and Indian summer monsoons to mountain
985 uplift shown by regional climate modelling experiments. Clim. Dyn. *40*, 1531–1549.

986 Tao, S., and Chen, L. (1987). A review of recent research on the East Asian summer
987 monsoon in China. In C.-P. Chang and T. N. Krishnamurti (eds): Monsoon
988 Meteorology, (London: Oxford University Press), pp. 60–92.

989 Tomita, T., Yamaura, T., and Hashimoto, T. (2011). Interannual Variability of the
990 Baiu Season near Japan Evaluated from the Equivalent Potential Temperature. J.
991 Meteorol. Soc. Jpn. Ser II *89*, 517–537.

992 Vertenstein, M., Craig, T., Middleton, A., Feddema, D., and Fischer, C. (2011).
993 CESM1.0.4 User's Guide.

994 Wang, S., and Zuo, H. (2016). Effect of the East Asian Westerly Jet's Intensity on
995 Summer Rainfall in the Yangtze River Valley and Its Mechanism. J. Clim. *29*, 2395–
996 2406.

997 Wang, B., Bao, Q., Hoskins, B.J., and Liu, Y. (2008). Tibetan Plateau warming and
998 precipitation changes in East Asia. Geophys. Res. Lett. *35*.

999 Wong, K.C., Liu, S., Turner, A.G., and Schiemann, R.K. (2018). Different Asian
1000 Monsoon Rainfall Responses to Idealized Orography Sensitivity Experiments in the
1001 HadGEM3-GA6 and FGOALS-FAMIL Global Climate Models. Adv. Atmospheric Sci. *35*,
1002 1049–1062.

1003 Wu, G., Liu, Y., He, B., Bao, Q., Duan, A., and Jin, F.-F. (2012). Thermal Controls on the
1004 Asian Summer Monsoon. Sci. Rep. *2*, 404.

1005 Xie, Z., Du, Y., and Yang, S. (2015). Zonal Extension and Retraction of the Subtropical
1006 Westerly Jet Stream and Evolution of Precipitation over East Asia and the Western
1007 Pacific. J. Clim. *28*, 6783–6798.

1008 Yanai, M., and Wu, G.-X. (2006). Effects of the Tibetan Plateau. In The Asian
1009 Monsoon, (Springer, Berlin, Heidelberg), pp. 513–549.

Accepted for publication in *Journal of Climate*. DOI 10.1175/JCLI-D-19-0319.1.

Yatagai, A., Arakawa, O., Kamiguchi, K., Kawamoto, H., Nodzu, M.I., and Hamada, A. (2009). A 44-Year Daily Gridded Precipitation Dataset for Asia Based on a Dense Network of Rain Gauges. Sola *5*, 137–140.

Yeh, T.-C., Dao, S.-Y., and Li, M.-T. (1959). The abrupt change of circulation over the Northern Hemisphere during June and October. In The Atmosphere and the Sea in Motion, (Rockefeller Institute Press), pp. 249–267.

Zhang, G.J., and McFarlane, N.A. (1995). Sensitivity of climate simulations to the parameterization of cumulus convection in the Canadian climate centre general circulation model. Atmosphere-Ocean *33*, 407–446.

Zhang, R., Jiang, D., Liu, X., and Tian, Z. (2012). Modeling the climate effects of different subregional uplifts within the Himalaya-Tibetan Plateau on Asian summer monsoon evolution. Chin. Sci. Bull. *57*, 4617–4626.

List of Figures

Figure 1.

Climatology of the 1979-2007 APHRODITE daily precipitation rate (unit: mm/day) in East Asia. (a) Temporal and (b)-(f) spatial patterns of EASM derived from the SOMs analysis of the APHRODITE dataset. Patterns1-5 (shown in panels (b) - (f)) are respectively the spring persistent rainfall (April 1st – June 3rd), pre-mei-yu (June 4th – June 22nd), mei-yu (June 23rd – July 20th), midsummer (July 21st – September 4th), and retreat of the EASM (September 5th – September 30th). (g) Hovmoller diagram of precipitation rate averaged from 110° to 120°E. Dashed lines in (g) denote timings of seasonal transitions based on the SOMs analysis.

Figure 2.

Climatological meridional gradient of equivalent potential temperature $\left(-\frac{\partial \theta_e}{\partial y}\right)$ (unit: 3×10^{-6} K/m) and meridional gradient of specific humidity $(-\frac{\partial q}{\partial y})$ (unit: 3×10^{-9} kg/kg/m) over 1979-2007. (a) Hovmoller diagram of $-\frac{\partial \theta_e}{\partial y}$ at 850mb in East China $(110°E - 120°E)$. Black dashed lines indicate SOMs derived timings for mei-yu and midsummer. Vertical cross-sections of $-\frac{\partial \theta_e}{\partial y}$ over $110° - 120°E$ in (b) mei-yu and (c) midsummer. Vertical cross-sections of $-\frac{\partial q}{\partial y}$ over $110° - 120°E$ in (d) mei-yu and (e) midsummer.

Figure 3.

Accepted for publication in *Journal of Climate*. DOI 10.1175/JCLI-D-19-0319.1.

Climatological vertical velocity (ω) over 1979-2007. (a) Hovmoller diagram of ω at 500mb in East China ($110°E - 120°E$). Black dashed lines indicate SOMs derived timings for mei-yu and midsummer. Spatial patterns of ω at 500mb in (b) mei-yu and (c) midsummer. Vertical cross-sections of ω over $110° - 120°E$ in (d) mei-yu and (e) midsummer. Unit: $-Pa/s$. Warm color indicates ascent.

Figure 4.

(a-e) Zonal wind and (f-j) meridional wind characteristics over East Asia associated with the mei-yu and midsummer stages (unit: m/s). Hovmoller diagram of (a) zonal wind at 200mb averaged over $80° - 100°E$ and (f) meridional wind at 500mb averaged over $110° - 120°E$; vertical dashed lines in (a) and (f) indicate SOMs derived timings for mei-yu and midsummer, and blue crosses in (a) indicate the latitude position of maximum westerlies for each day. Maps of (b)-(c) zonal wind at 200mb and (g)-(h) meridional wind at 500mb, for (b), (g) mei-yu and (c), (h) midsummer. Pressure-latitude ($20° - 50°N$) cross section of (d)-(e) zonal wind averaged over $80° - 100°E$ and (i)-(j) meridional wind averaged over $110° - 120°E$, for (d), (i) mei-yu and (e), (j) midsummer. Grey shadings indicate zonally averaged topography in (d)-(e) over $80° - 100°E$ and (i)-(j) over $110° - 120°E$. Black contours in (b)-(c), (g)-(h) indicate elevation of 2000 m.

Figure 5.

(a)-(b) Matched timings for 9 day running averaged daily climatology, for (a) high years and (b) low years. Y-axes in (a)-(b) labels spring as 1, pre mei-yu as 2, mei-yu as 3, midsummer as 4, and end of the EASM season as 5. (c)-(j) Hovmoller diagrams for high years (left panels), and low years (right panels): (c)-(d) meridional gradient of 850mb equivalent potential temperature $\left(-\frac{\partial \theta_e}{\partial y}\right)$ averaged over $110° - 120°E$ (unit: 3×10^{-6} K/m); (e)-(f) ascending motion averaged over $110° - 120°E$ at 500mb (unit: $-Pa/s$); (g)-(h) zonal wind at 200mb averaged over $80° - 100°E$ (unit: m/s); (i)-(j) meridional wind at 500mb averaged over $110° - 120°E$ (unit: m/s). Black dashed lines in the left panel indicate matched mei-yu period for high years, and black dashed lines in the right panel indicate matched mei-yu period for low years. To remove weather noise, we applied a 9-day running mean to fields shown in (c)-(j).

Figure 6.

(a) Timings of matched SOMs patterns for each pentad from April 1st through September 27th in 1979-2007 (blue lines), overlaid with climatological SOMs patterns (red lines). (b) Temporal density of matched

Accepted for publication in *Journal of Climate*. DOI 10.1175/JCLI-D-19-0319.1.

SOMs patterns shown in (a); for each pentad at Y-axis, color for a corresponding SOMs pattern indicates number of pentads in 1979-2007 April-September that are matched to that pattern. (c) Density of jet positions, where jet position is defined as latitude of maximum westerlies at 200mb in Tibet region; for each SOMs pattern, colors indicate number of pentads when jet is located at a certain latitude. (d) Density of strength of meridional wind at 500mb averaged in $(110° - 120°E, 35° - 40°N)$; for each SOMs pattern, colors indicate number of pentads when the strength of meridional wind is between a certain range as indicated on Y-axis. (e) Jet position for each pentad in April through September from 1979 to 2007 (blue lines), overlaid with climatological jet position in 1979-2007. (f) SOM pattern density; for each jet position, colors indicate number of corresponding pentads that are matched to a certain SOMs pattern. (g) Density of strength of V; for each jet position, colors indicate number of pentads when strength of V falls in a certain interval as indicated on Y-axis. Note that Fig. 6f is identical to Fig. 6c by construction, we show both here for clarity.

Figure 7.

Composites based on pentads when latitude of the zonal wind maximum impinging on the Tibetan Plateau is (left) $37°N$, (middle) $40°N$ and (right) $43°N$. The pentads are taken from April through September, for years 1979-2007. (a)-(c) Zonal wind at 200mb (unit: m/s); (d)-(f) Meridional wind at 500mb (unit: m/s); (g)-(i) Meridional gradient of equivalent potential temperature $\left(-\frac{\partial \theta_e}{\partial y}\right)$ (unit: 3×10^{-6} K/m); (j)-(l) APHRODITE rain gauge data (unit: mm/day). Black contours in (a)-(c) indicate elevation of 2000 m.

Figure 8.

The meridional MSE flux ($vh; h = C_pT + L_vq + gz$) (unit: $10^3 kJ/kg \cdot m/s$) (upper row), and the meridional wind convergence ($-\frac{\partial v}{\partial y}$) (unit: $10^{-6}s^{-1}$) (bottom row). Results are shown for hovmoller diagram of vertical integrations (1000mb to 250mb) averaged over $110° - 120°E$ (left column), differences of vertical integrations (1000mb to 250mb) between mei-yu and midsummer (mei-yu minus midsummer) (middle column), and differences of averaged values over $110° - 120°E$ between mei-yu and midsummer (mei-yu minus midsummer) (right column). Grey shadings in (c), (f) indicate zonally averaged topography over $110° - 120°E$. Black contours in (b), (e) indicate elevation of 2000 m.

Figure 9.

Accepted for publication in *Journal of Climate*. DOI 10.1175/JCLI-D-19-0319.1.

Climatological changes in the mass-weighted vertical integral (from 1000mb to 100mb) of moisture budget components between mei-yu and midsummer (mei-yu minus midsummer). Vectors denote moisture fluxes (unit: m^2/s), and color shadings denote moisture flux convergence (unit: mm/day; cold color indicates convergence, and warm color indicates divergence). (a) Changes of moisture flux and its convergence. (b) Contributions by the changes of specific humidity. (c) Contributions by changes of horizontal winds. (d) Contributions by changes of both specific humidity and horizontal winds. (e) Contributions by changes of transients. (f) Contributions by changes to the zonal moisture flux and its convergence. (g) Contributions by changes to the meridional moisture flux and its convergence. (g) is contributed from two terms, with (h) shows the contributions by meridional wind convergence, and (i) shows contributions by meridional advection of moisture.

Figure 10.

Similar to Figure 9, but for comparison between high years and low years during July 3rd (timing of mei-yu termination in high years) to July 23rd (timing of mei-yu termination in low years). Here, changes denote low years minus high years.

Figure 11.

Results from the "Plateau_control" (the first column), the "Plateau_3deg" (the second column), the "Plateau_6deg" (the third column) and the "Plateau_10deg" (the fourth column). (a)-(h) Hovmoller diagram of (a)-(d) zonal wind at 200mb averaged over $80° - 100°E$ and (e)-(h) meridional wind at 500mb averaged over $110° - 120°E$ (units: m/s). (i)-(l) Hovmoller diagram of meridional gradient of θ_e at 850mb and over $110° - 120°E$ (units: 3×10^{-6} K/m). (m)-(t) Large-scale precipitation averaged in (m)-(p) June and in (q)-(t) July (units: mm/day). Black contours in (m)-(t) indicate elevation of 2000 m.

Figure 12.

Results from the dry dynamical core simulations "PlateauN6" (the first column), "PlateauN3" (the second column), "Plateau" (the third column), "PlateauS3" (the fourth column), and "PlateauS6" (the fifth column). (a)-(e) Zonal wind at 200mb; (f)-(j) Meridional wind at 500mb; (k)-(o) Zonal wind averaged in $80° - 100°E$; (p)-(t) Meridional wind averaged in $110° - 120°E$. Black contours in (a)-(j) indicate elevation of 2000 m.

Figure 13.

Accepted for publication in *Journal of Climate*. DOI 10.1175/JCLI-D-19-0319.1.

(top) Eddy geopotential height at 500mb (units: meters) and (bottom) Horizontal EP flux (vectors; units: m^2/s^2) and quasi-geostrophic eddy streamfunction (color shading; units: 10^6 s^{-1}) at 250mb from the idealized simulations. (a), (d) "Plateau", (b), (e)"PlateauS3" and (c), (f) "PlateauS6". Black solid lines denote imposed topography. (g) The ratio of the meridional component of the EP flux to the zonal component of the EP flux at 250mb averaged in $25° - 45°N, 100° - 150°E$. Black solid lines in (a)-(f) denote imposed topography and indicate elevation of 2000 m. Green dashed lines in (d)-(f) denote the area used for the calculation of (g).

Figure 14.

Eddy geopotential height at 500mb (units: meter) over 1979-2007 during (a) mei-yu, (b) midsummer, and (c) midsummer minus mei-yu. Timing of mei-yu and midsummer is determined by the SOMs analysis. Dashed lines indicate the longitudinal range used for zonal average shown in Figure 15. Black contours indicate elevation of 2000 m.

Figure 15.

Hovmoller diagram of eddy geopotential height averaged in $110° - 150°E$ at (a)-(c) 200mb and at (d)-(f) 500mb for 1979-2007 climatology (left), high year climatology (middle) and low year climatology (right). Black dashed lines in (a)-(f) demarcate pre-mei-yu, mei-yu, midsummer, and end periods, respectively.

Figure A1.

Boundary topography for the "Plateau_control" run in (a), (e) and the extended Plateau simulations in (b)-(d) and (f)-(h). The upper row presents distribution of topography in East Asia, and the lower row presents the vertical cross section of elevation averaged in $80° - 100°E$. Unit: meters.

Figure A2.

The (a) first EOF and (b) principal component of July-August mean precipitation over East Asia $(100° - 145°E, 20° - 45°N)$. The spatial pattern is the regression of the normalized PC1 onto the July-August rainfall anomaly (units are mm/day per standard deviation). The first mode is the well-known "tripole pattern" (Hsu and Lin, 2007) with reduced rainfall over central eastern China and Japan and increased rainfall over northeastern and southeastern China. We use the APHRODITE dataset spanning 1951-2007. The mode explains 17.7% of the total variance. Adopted from (Chiang et al., 2017) and reproduced based on Figs. 1b-c of (Chiang et al., 2017).

Accepted for publication in *Journal of Climate*. DOI 10.1175/JCLI-D-19-0319.1.

1149

1150

1151

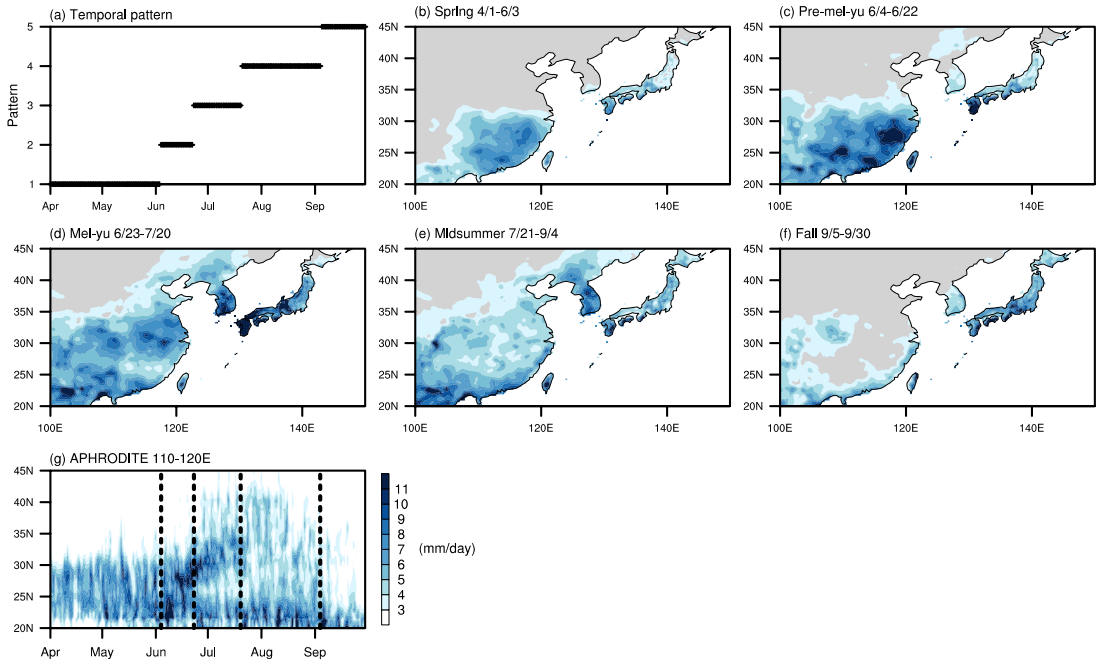

1152

1153 **Figure 1.** Climatology of the 1979-2007 APHRODITE daily precipitation rate (unit: mm/day) in East Asia.

1154 (a) Temporal and (b)-(f) spatial patterns of EASM derived from the SOMs analysis of the APHRODITE

1155 dataset. Patterns1-5 (shown in panels (b) - (f)) are respectively the spring persistent rainfall (April 1st – June

1156 3rd), pre-mei-yu (June 4th – June 22nd), mei-yu (June 23rd – July 20th), midsummer (July 21st – September

1157 4th), and retreat of the EASM (September 5th – September 30th). (g) Hovmoller diagram of precipitation rate

Accepted for publication in *Journal of Climate*. DOI 10.1175/JCLI-D-19-0319.1.

averaged from 110° to 120°E. Dashed lines in (g) denote timings of seasonal transitions based on the SOMs analysis.

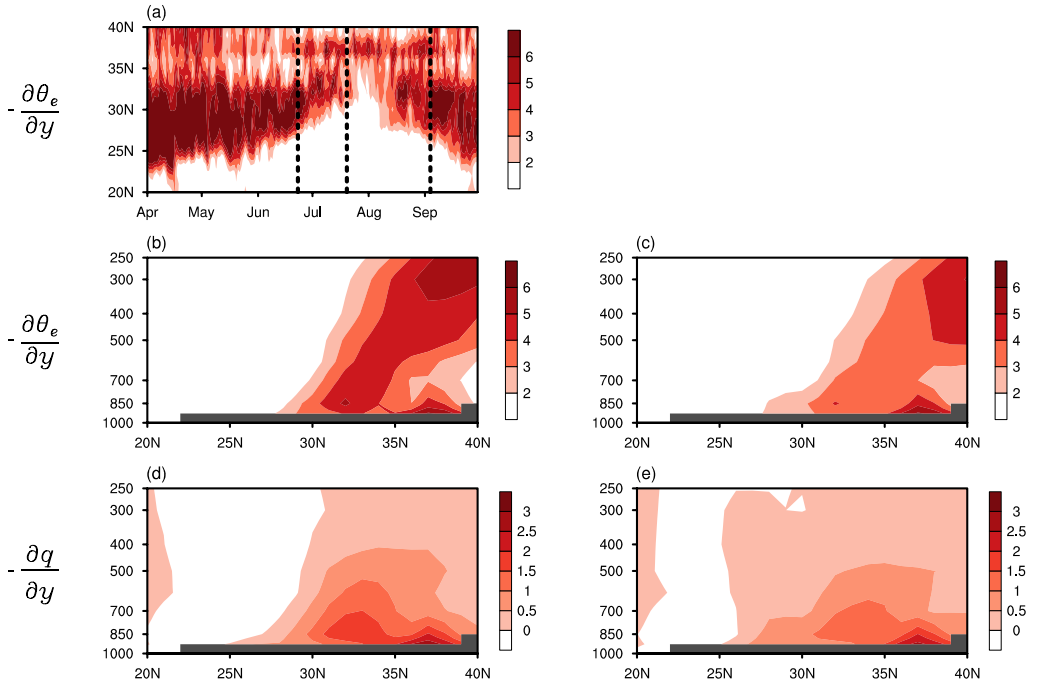

Figure 2. Climatological meridional gradient of equivalent potential temperature $\left(-\frac{\partial \theta_e}{\partial y}\right)$ (unit: 3×10^{-6} K/m) and meridional gradient of specific humidity $\left(-\frac{\partial q}{\partial y}\right)$ (unit: 3×10^{-9} kg/kg/m) over 1979-2007. (a) Hovmoller diagram of $-\frac{\partial \theta_e}{\partial y}$ at 850mb in East China ($110°E - 120°E$). Black dashed lines indicate SOMs

Accepted for publication in *Journal of Climate*. DOI 10.1175/JCLI-D-19-0319.1.

derived timings for mei-yu and midsummer. Vertical cross-sections of $-\frac{\partial \theta_e}{\partial y}$ over $110° - 120°E$ in (b) mei-yu and (c) midsummer. Vertical cross-sections of $-\frac{\partial q}{\partial y}$ over $110° - 120°E$ in (d) mei-yu and (e) midsummer.

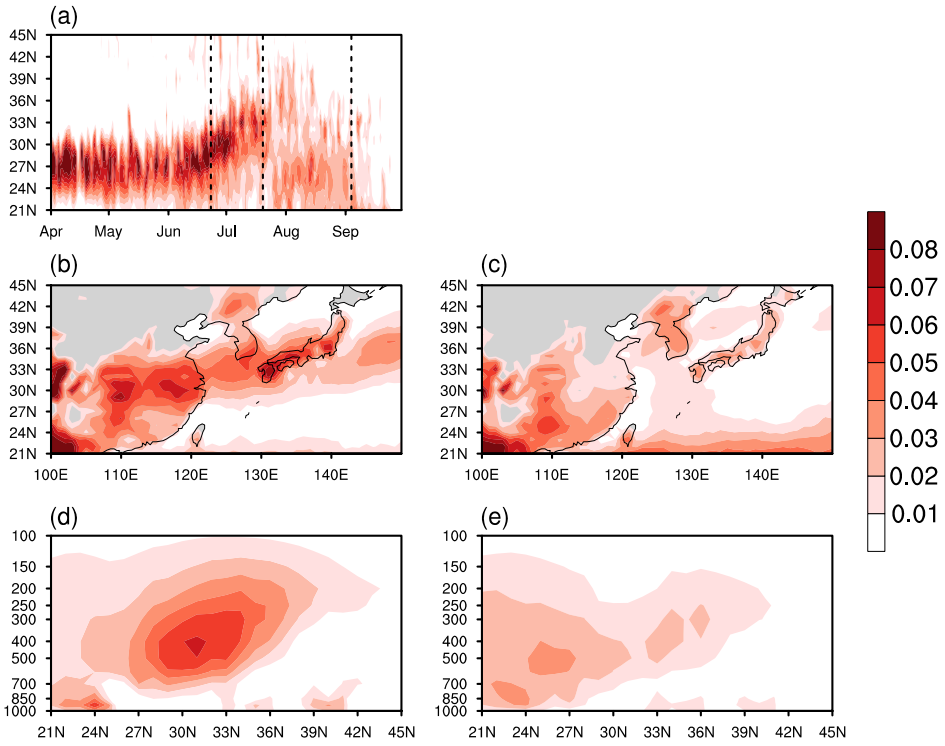

Figure 3. Climatological vertical velocity (ω) over 1979-2007. (a) Hovmoller diagram of ω at 500mb in East China ($110°E - 120°E$). Black dashed lines indicate SOMs derived timings for mei-yu and midsummer. Spatial patterns of ω at 500mb in (b) mei-yu and (c) midsummer. Vertical cross-sections of ω over $110° - 120°E$ in (d) mei-yu and (e) midsummer. Unit: $-Pa/s$. Warm color indicates ascent.

Accepted for publication in *Journal of Climate*. DOI 10.1175/JCLI-D-19-0319.1.

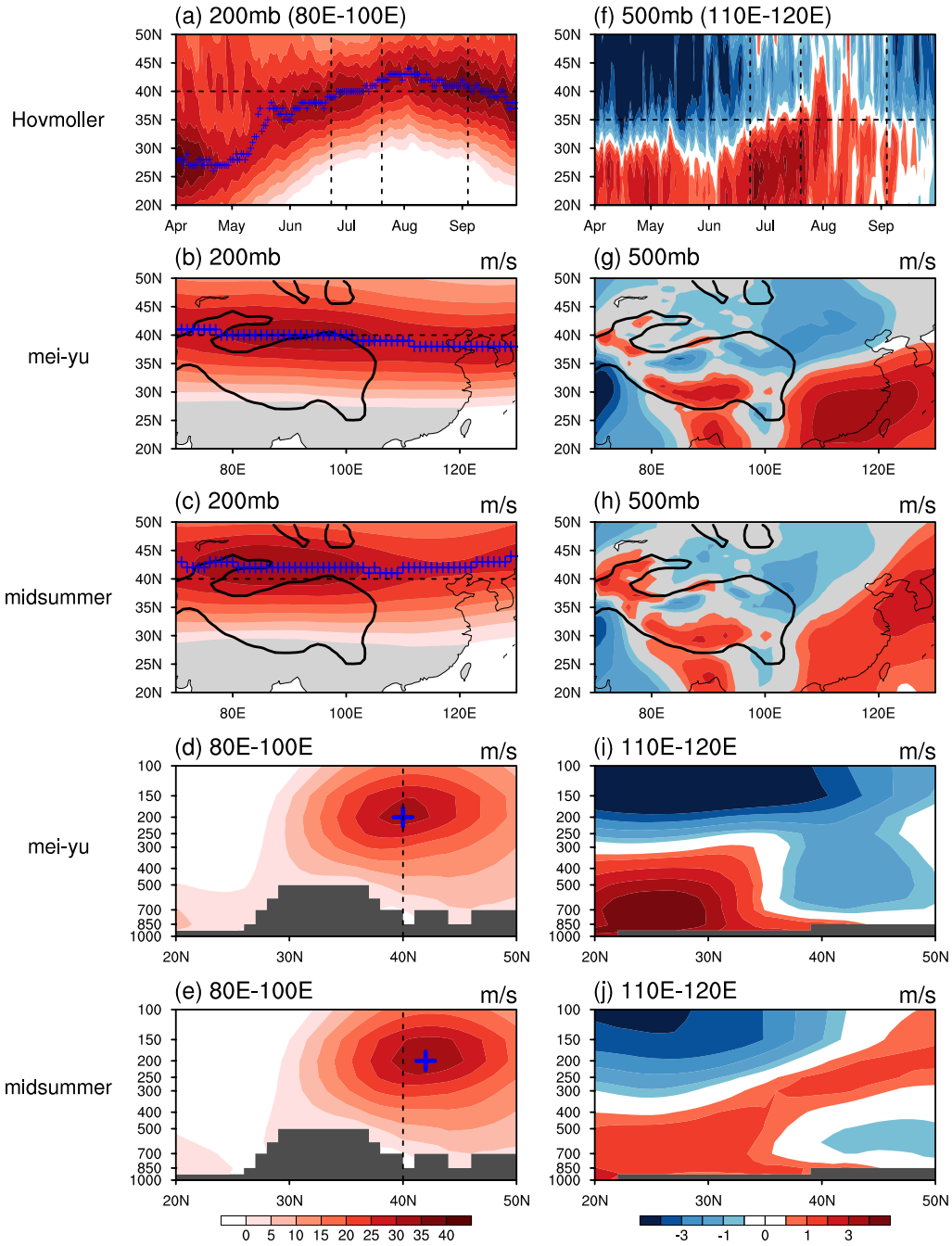

Figure 4. (a-e) Zonal wind and (f-j) meridional wind characteristics over East Asia associated with the mei-yu and midsummer stages (unit: m/s). Hovmoller diagram of (a) zonal wind at 200mb averaged over $80° - 100°E$ and (f) meridional wind at 500mb averaged over $110° - 120°E$; vertical dashed lines in (a) and (f) indicate SOMs derived timings for mei-yu and midsummer, and blue crosses in (a) indicate the latitude

Accepted for publication in *Journal of Climate*. DOI 10.1175/JCLI-D-19-0319.1.

position of maximum westerlies for each day. Maps of (b)-(c) zonal wind at 200mb and (g)-(h) meridional wind at 500mb, for (b), (g) mei-yu and (c), (h) midsummer. Pressure-latitude ($20° - 50°N$) cross section of (d)-(e) zonal wind averaged over $80° - 100°E$ and (i)-(j) meridional wind averaged over $110° - 120°E$, for (d), (i) mei-yu and (e), (j) midsummer. Grey shadings indicate zonally averaged topography in (d)-(e) over $80° - 100°E$ and (i)-(j) over $110° - 120°E$. Black contours in (b)-(c), (g)-(h) indicate elevation of 2000 m.

Accepted for publication in *Journal of Climate*. DOI 10.1175/JCLI-D-19-0319.1.

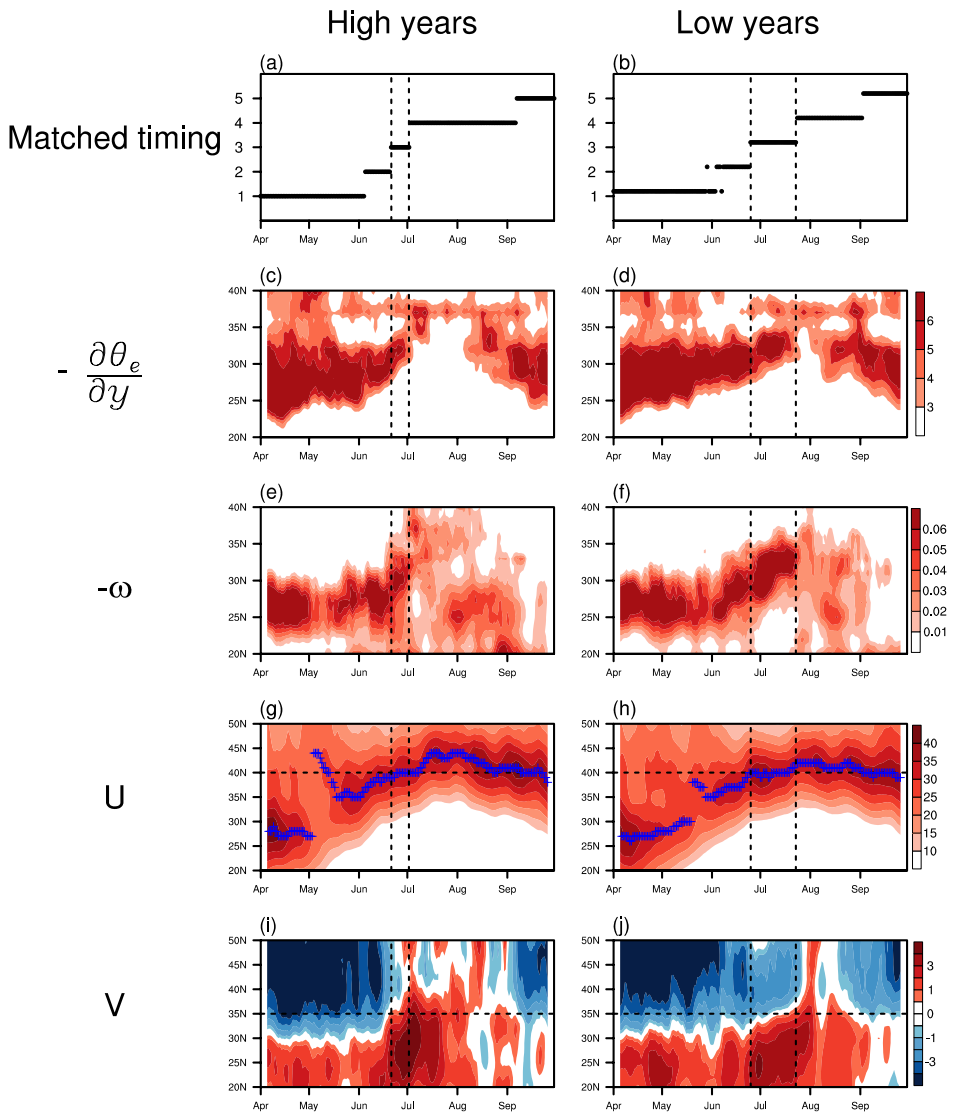

Figure 5. (a)-(b) Matched timings for 9 day running averaged daily climatology, for (a) high years and (b) low years. Y-axes in (a)-(b) labels spring as 1, pre mei-yu as 2, mei-yu as 3, midsummer as 4, and end of the EASM season as 5. (c)-(j) Hovmoller diagrams for high years (left panels), and low years (right panels): (c)-(d) meridional gradient of 850mb equivalent potential temperature $\left(-\frac{\partial \theta_e}{\partial y}\right)$ averaged over $110° - 120°E$ (unit: 3×10^{-6} K/m); (e)-(f) ascending motion averaged over $110° - 120°E$ at 500mb (unit: $-Pa/s$); (g)-(h) zonal wind at 200mb averaged over $80° - 100°E$ (unit: m/s); (i)-(j) meridional wind at 500mb averaged over $110° - 120°E$ (unit: m/s). Black dashed lines in the left panel indicate matched mei-yu

Accepted for publication in *Journal of Climate*. DOI 10.1175/JCLI-D-19-0319.1.

period for high years, and black dashed lines in the right panel indicate matched mei-yu period for low years. To remove weather noise, we applied a 9-day running mean to fields shown in (c)-(j).

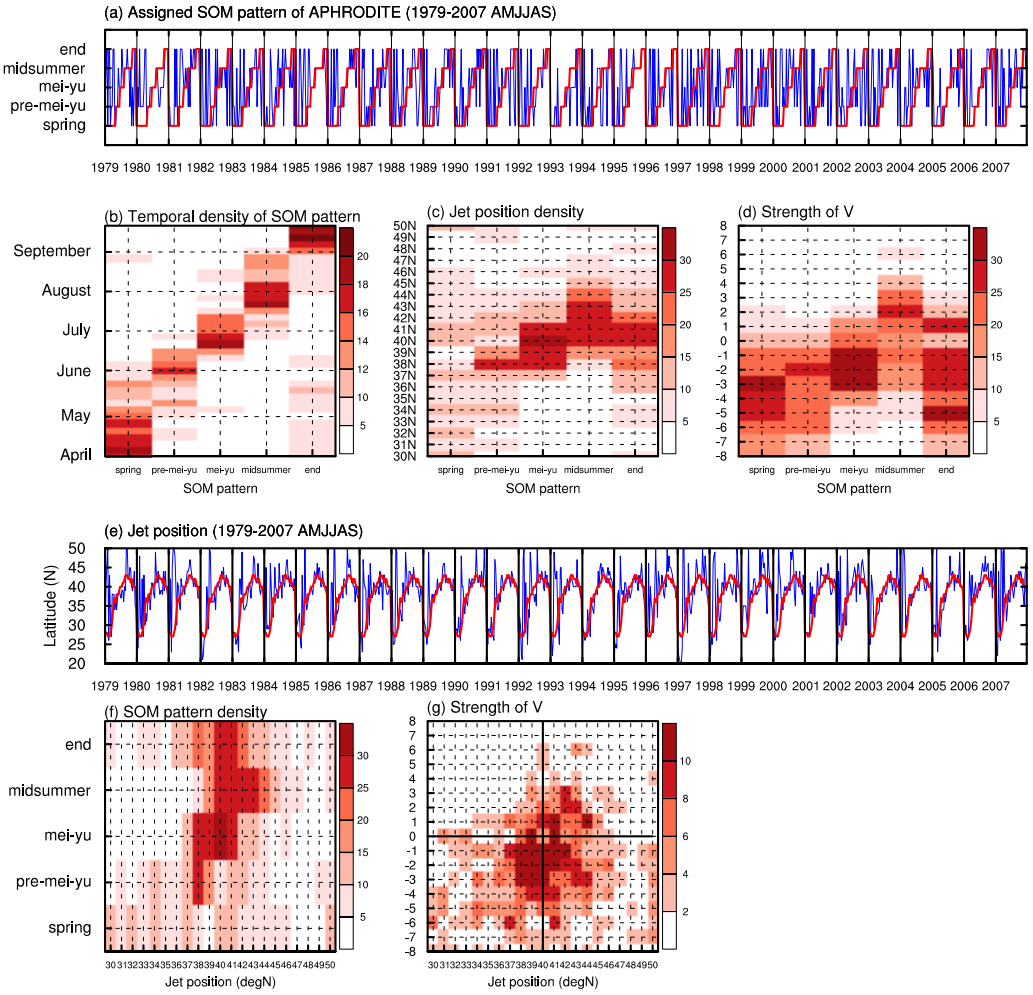

Figure 6. (a) Timings of matched SOMs patterns for each pentad from April 1st through September 27th in 1979-2007 (blue lines), overlaid with climatological SOMs patterns (red lines). (b) Temporal density of matched SOMs patterns shown in (a); for each pentad at Y-axis, color for a corresponding SOMs pattern indicates number of pentads in 1979-2007 April-September that are matched to that pattern. (c) Density of jet positions, where jet position is defined as latitude of maximum westerlies at 200mb in Tibet region; for each SOMs pattern, colors indicate number of pentads when jet is located at a certain latitude. (d) Density

Accepted for publication in *Journal of Climate*. DOI 10.1175/JCLI-D-19-0319.1.

of strength of meridional wind at 500mb averaged in $(110° - 120°E, 35° - 40°N)$; for each SOMs pattern, colors indicate number of pentads when the strength of meridional wind is between a certain range as indicated on Y-axis. (e) Jet position for each pentad in April through September from 1979 to 2007 (blue lines), overlaid with climatological jet position in 1979-2007. (f) SOM pattern density; for each jet position, colors indicate number of corresponding pentads that are matched to a certain SOMs pattern. (g) Density of strength of V; for each jet position, colors indicate number of pentads when strength of V falls in a certain interval as indicated on Y-axis. Note that Fig. 6f is identical to Fig. 6c by construction, we show both here for clarity.

Accepted for publication in *Journal of Climate*. DOI 10.1175/JCLI-D-19-0319.1.

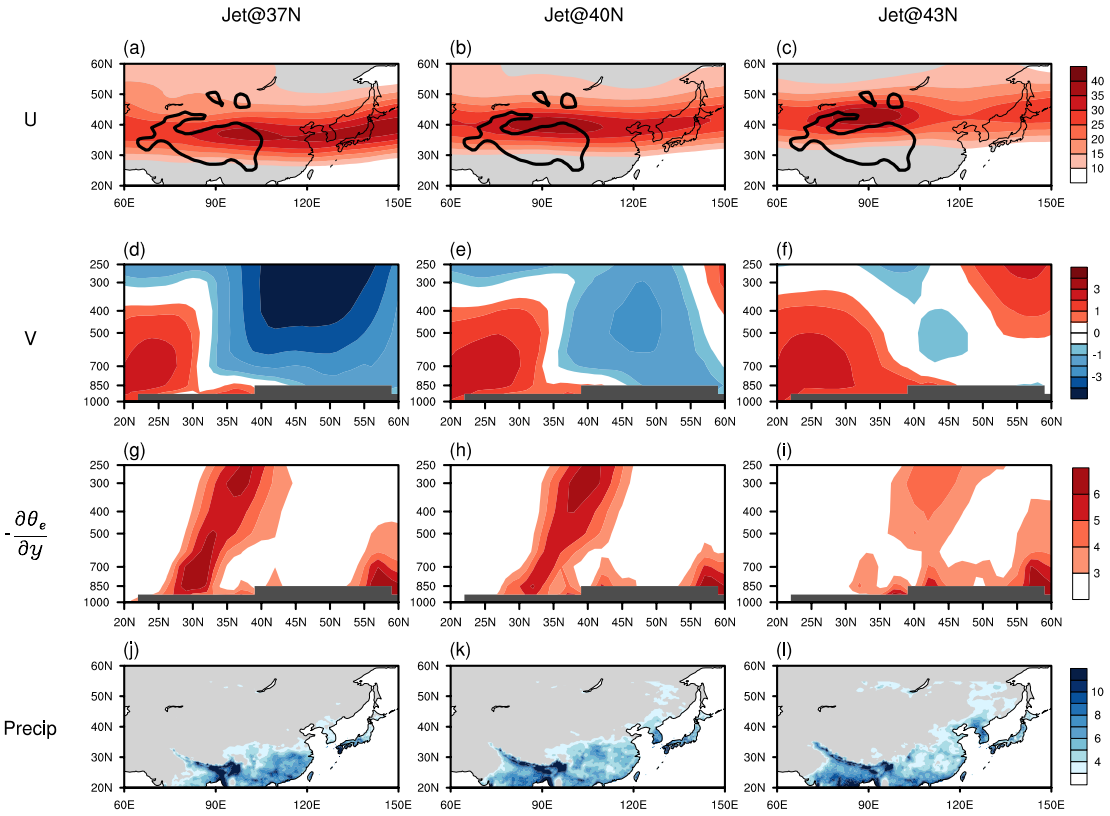

Figure 7. Composites based on pentads when latitude of the zonal wind maximum impinging on the Tibetan Plateau is (left) $37°N$, (middle) $40°N$ and (right) $43°N$. The pentads are taken from April through September, for years 1979-2007. (a)-(c) Zonal wind at 200mb (unit: m/s); (d)-(f) Meridional wind at 500mb (unit: m/s); (g)-(i) Meridional gradient of equivalent potential temperature $\left(-\frac{\partial \theta_e}{\partial y}\right)$ (unit: 3×10^{-6} K/m); (j)-(l) APHRODITE rain gauge data (unit: mm/day). Black contours in (a)-(c) indicate elevation of 2000 m.

Accepted for publication in *Journal of Climate*. DOI 10.1175/JCLI-D-19-0319.1.

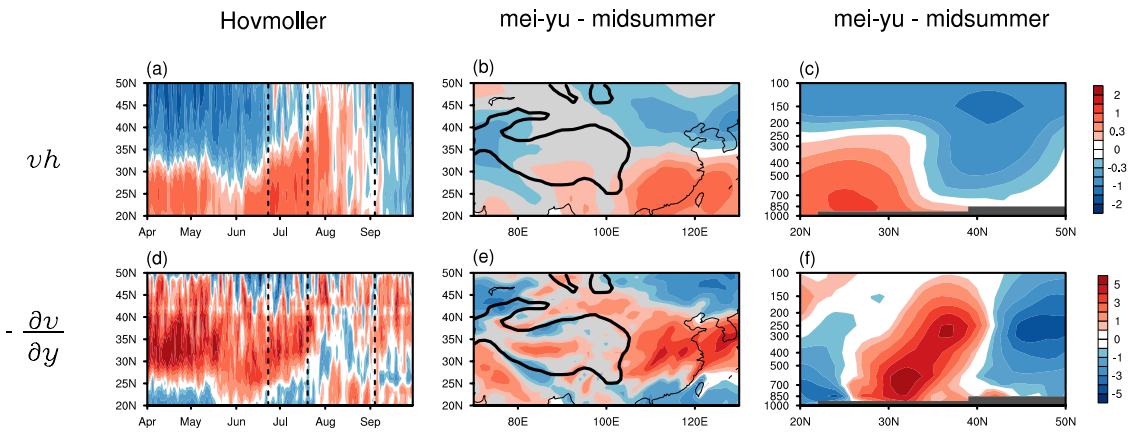

Figure 8. The meridional MSE flux ($vh; h = C_pT + L_vq + gz$) (unit: $10^3 kJ/kg \cdot m/s$) (upper row), and the meridional wind convergence ($-\frac{\partial v}{\partial y}$) (unit: $10^{-6}s^{-1}$) (bottom row). Results are shown for hovmoller diagram of vertical integrations (1000mb to 250mb) averaged over $110° - 120°E$ (left column), differences of vertical integrations (1000mb to 250mb) between mei-yu and midsummer (mei-yu minus midsummer) (middle column), and differences of averaged values over $110° - 120°E$ between mei-yu and midsummer (mei-yu minus midsummer) (right column). Grey shadings in (c), (f) indicate zonally averaged topography over $110° - 120°E$. Black contours in (b), (e) indicate elevation of 2000 m.

Accepted for publication in *Journal of Climate*. DOI 10.1175/JCLI-D-19-0319.1.

1241

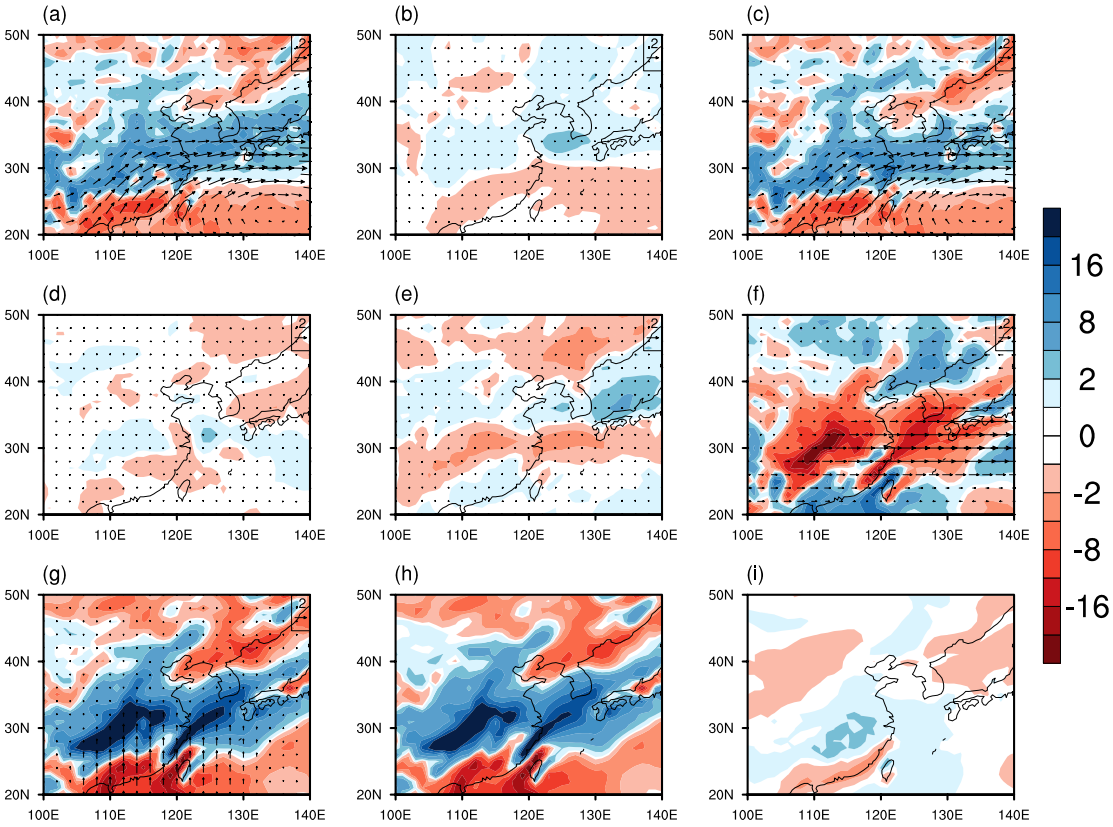

1242

1243 **Figure 9.** Climatological changes in the mass-weighted vertical integral (from 1000mb to 100mb) of
1244 moisture budget components between mei-yu and midsummer (mei-yu minus midsummer). Vectors denote
1245 moisture fluxes (unit: m^2/s), and color shadings denote moisture flux convergence (unit: mm/day; cold
1246 color indicates convergence, and warm color indicates divergence). (a) Changes of moisture flux and its
1247 convergence. (b) Contributions by the changes of specific humidity. (c) Contributions by changes of
1248 horizontal winds. (d) Contributions by changes of both specific humidity and horizontal winds. (e)
1249 Contributions by changes of transients. (f) Contributions by changes to the zonal moisture flux and its
1250 convergence. (g) Contributions by changes to the meridional moisture flux and its convergence. (g) is

Accepted for publication in *Journal of Climate*. DOI 10.1175/JCLI-D-19-0319.1.

contributed from two terms, with (h) shows the contributions by meridional wind convergence, and (i) shows contributions by meridional advection of moisture.

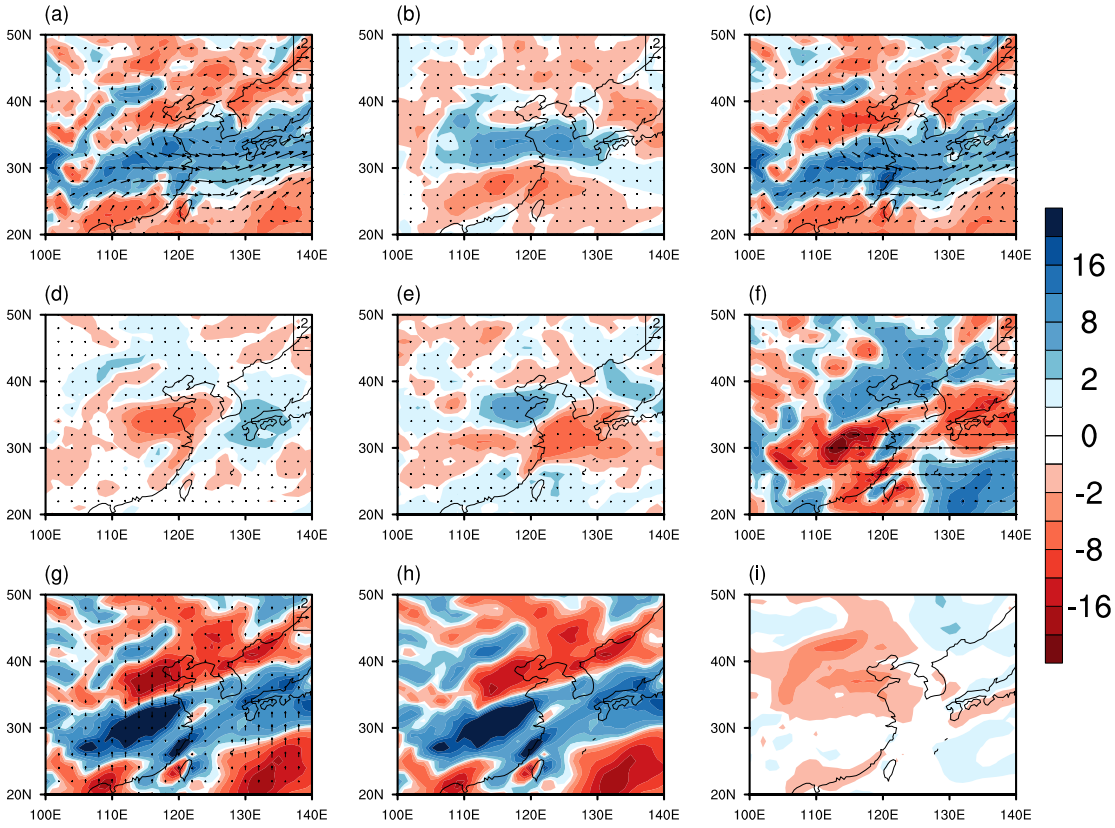

Figure 10. Similar to Figure 9, but for comparison between high years and low years during July 3rd (timing of mei-yu termination in high years) to July 23rd (timing of mei-yu termination in low years). Here, changes denote low years minus high years.

Accepted for publication in *Journal of Climate*. DOI 10.1175/JCLI-D-19-0319.1.

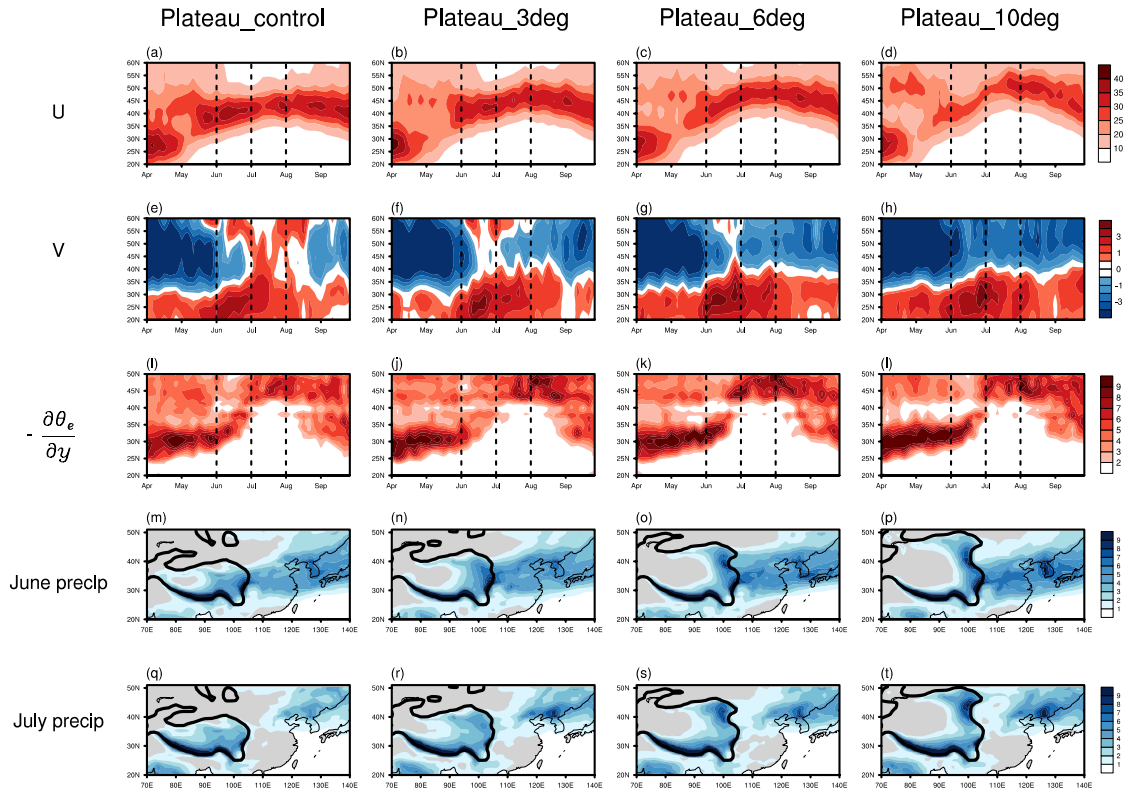

Figure 11. Results from the "Plateau_control" (the first column), the "Plateau_3deg" (the second column), the "Plateau_6deg" (the third column) and the "Plateau_10deg" (the fourth column). (a)-(h) Hovmoller diagram of (a)-(d) zonal wind at 200mb averaged over $80° - 100°E$ and (e)-(h) meridional wind at 500mb averaged over $110° - 120°E$ (units: m/s). (i)-(l) Hovmoller diagram of meridional gradient of θ_e at 850mb and over $110° - 120°E$ (units: 3×10^{-6} K/m). (m)-(t) Large-scale precipitation averaged in (m)-(p) June and in (q)-(t) July (units: mm/day). Black contours in (m)-(t) indicate elevation of 2000 m.

Accepted for publication in *Journal of Climate*. DOI 10.1175/JCLI-D-19-0319.1.

1268

1269

1270

1271

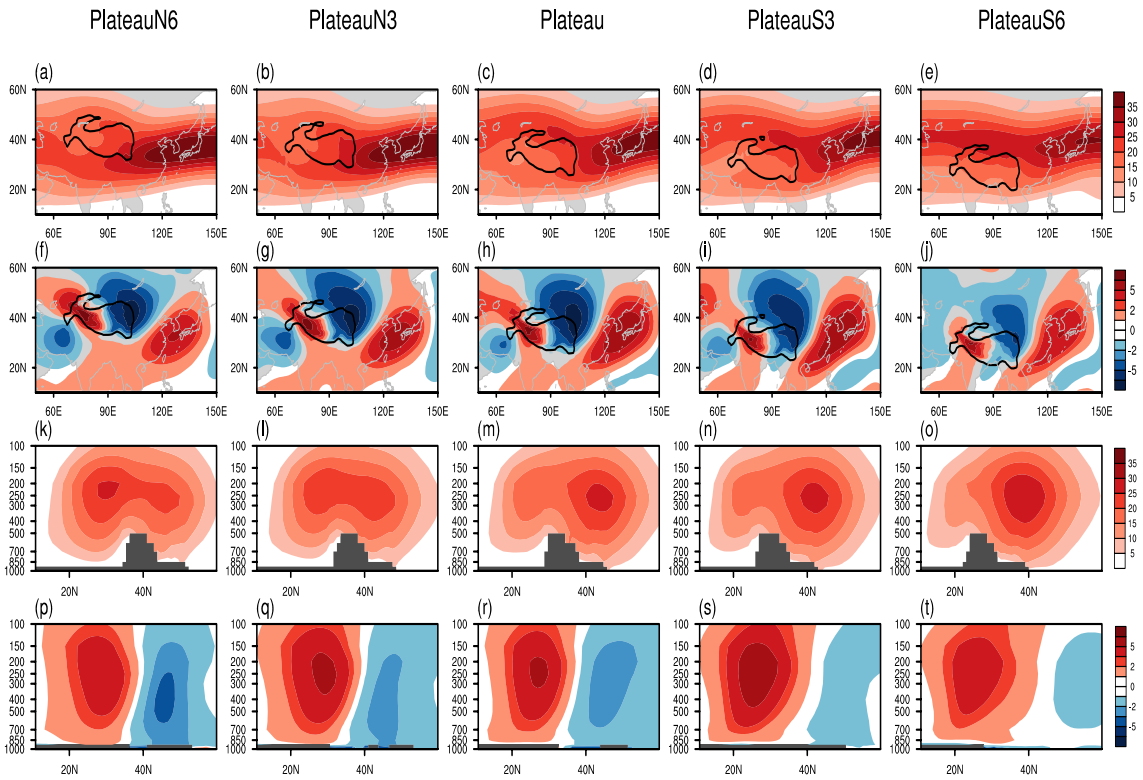

1272

1273

Accepted for publication in *Journal of Climate*. DOI 10.1175/JCLI-D-19-0319.1.

Figure 12. Results from the dry dynamical core simulations "PlateauN6" (first column), "PlateauN3" (second column), "Plateau" (third column), "PlateauS3" (fourth column), and "PlateauS6" (fifth column). (a)-(e) Zonal wind at 200mb; (f)-(j) Meridional wind at 500mb; (k)-(o) Zonal wind averaged in $80° - 100°E$; (p)-(t) Meridional wind averaged in $110° - 120°E$. Black contours in (a)-(j) indicate elevation of 2000 m.

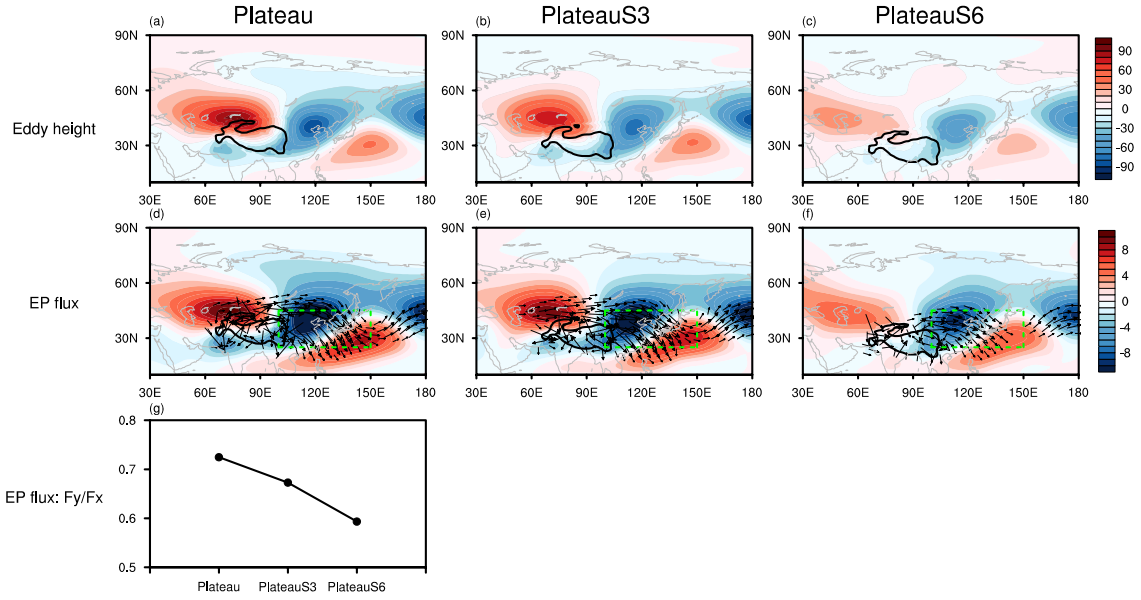

Figure 13. (top) Eddy geopotential height at 500mb (units: meters) and (bottom) Horizontal EP flux (vectors; units: m^2/s^2) and quasi-geostrophic eddy streamfunction (color shading; units: 10^6 s^{-1}) at 250mb

Accepted for publication in *Journal of Climate*. DOI 10.1175/JCLI-D-19-0319.1.

from the idealized simulations. (a), (d) “Plateau”, (b), (e)“PlateauS3” and (c), (f) “PlateauS6”. (g) The ratio of the meridional component of the EP flux to the zonal component of the EP flux at 250mb averaged in $25° - 45°N, 100° - 150°E$. Black solid lines in (a)-(f) denote imposed topography and indicate elevation of 2000 m. Green dashed lines in (d)-(f) denote the area used for the calculation of (g).

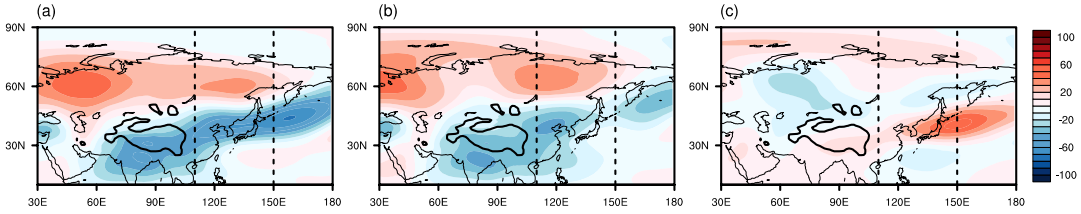

Figure 14. Eddy geopotential height at 500mb (units: meter) over 1979-2007 during (a) mei-yu, (b) midsummer, and (c) midsummer minus mei-yu. Timing of mei-yu and midsummer is determined by the

Accepted for publication in *Journal of Climate*. DOI 10.1175/JCLI-D-19-0319.1.

SOMs analysis. Dashed lines indicate the longitudinal range used for zonal average shown in Figure 15. Black contours indicate elevation of 2000 m.

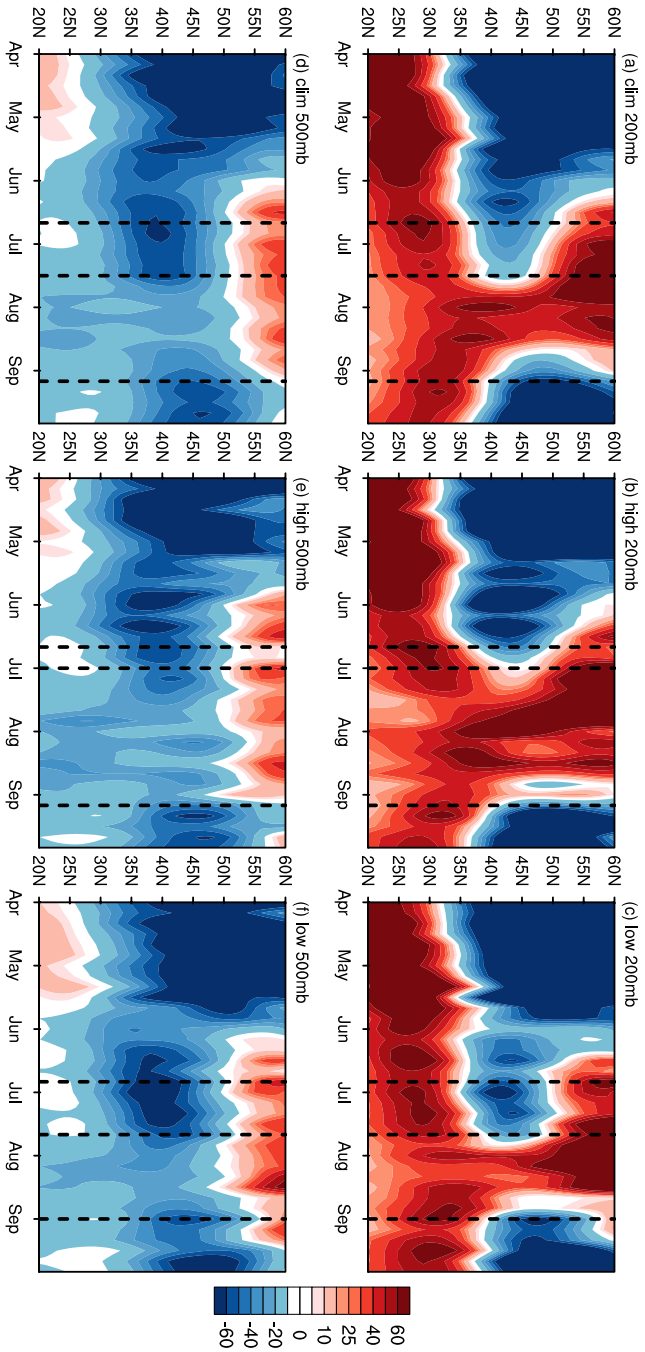

Figure 15. Hovmoller diagram of eddy geopotential height averaged in $110° - 150°E$ at (a)-(c) 200mb and at (d)-(f) 500mb for 1979-2007 climatology (left), high year climatology (middle) and low year

Accepted for publication in *Journal of Climate*. DOI 10.1175/JCLI-D-19-0319.1.

climatology (right). Black dashed lines in (a)-(f) demarcate pre-mei-yu, mei-yu, midsummer, and end periods, respectively.

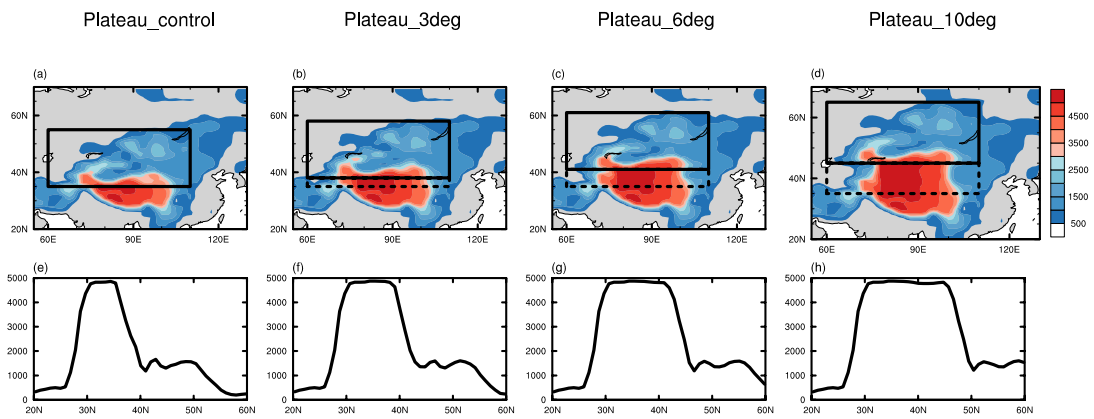

Figure A1. Boundary topography for the "Plateau_control" run in (a), (e) and the extended Plateau simulations in (b)-(d) and (f)-(h). The upper row presents distribution of topography in East Asia, and the lower row presents the vertical cross section of elevation averaged in $80° - 100°E$. Unit: meters.

Accepted for publication in *Journal of Climate*. DOI 10.1175/JCLI-D-19-0319.1.

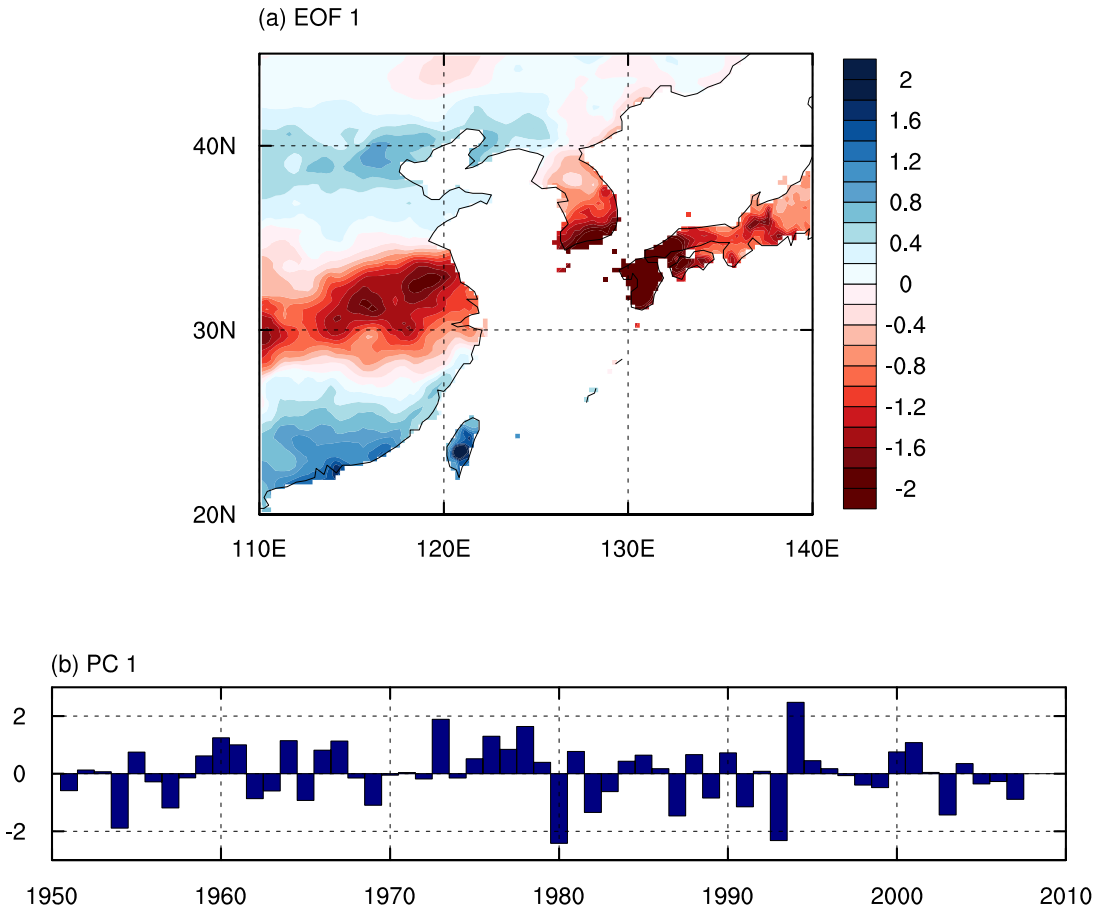

Figure A2. The (a) first EOF and (b) principal component of July-August mean precipitation over East Asia $(100° - 145°E, 20° - 45°N)$. The spatial pattern is the regression of the normalized PC1 onto the July-August rainfall anomaly (units are mm/day per standard deviation). The first mode is the well-known "tripole pattern" (Hsu and Lin, 2007) with reduced rainfall over central eastern China and Japan and increased rainfall over northeastern and southeastern China. We use the APHRODITE dataset spanning 1951-2007. The mode explains 17.7% of the total variance. Adopted from (Chiang et al., 2017) and reproduced based on Figs. 1b-c of (Chiang et al., 2017).

Accepted for publication in *Journal of Climate*. DOI 10.1175/JCLI-D-19-0319.1.